Development of the WRF-CO2 4DVar assimilation system v1.0

Tao Zheng[1,4], Nancy H.F. French[2], and Martin Baxter[3]

[1]Department of Geography, Central Michigan University, Mount Pleasant, MI. USA
[2]Michigan Tech Research Institute, Michigan Technological University, Ann Arbor, MI. USA
[3]Department of Earth and Atmospheric Sciences, Central Michigan University, Mount Pleasant, MI. USA
[4]Institute of Great Lakes Research, Central Michigan University, Mount Pleasant, MI. USA

Correspondence to: Tao Zheng (zheng1t@cmich.edu)

Abstract. Regional atmospheric CO_2 inversions commonly use Lagrangian particle trajectory model simulations to calculate the required influence function, which quantifies the sensitivity of a receptor to flux sources. In this paper, an adjoint based four-dimensional variational (4DVar) assimilation system, WRF-CO2 4DVar, is developed to provide an alternative approach. This system is developed based on the Weather Research and Forecasting (WRF) modeling system, including WRF-Chem, WRFPLUS, and WRFDA, all in version 3.6. In WRF-CO2 4DVar, CO_2 is modeled as a tracer and its feedback to meteorology is ignored. This configuration allows most WRF physical parameterizations to be used in the assimilation system without incurring a large amount of code development. WRF-CO2 4DVar solves for the optimized CO_2 emission scaling factors in a Bayesian framework. Two variational optimization schemes are implemented for the system: the first uses the L-BFGS-B and the second uses the Lanczos conjugate gradient (CG) in an incremental approach. WRFPLUS forward, tangent linear, and adjoint models are modified to include CO_2 related processes. The system is tested by simulations over a domain covering the continental United States at 48 km $\times$ 48 km grid spacing. The accuracy of the tangent linear and adjoint models are assessed by comparing against finite difference sensitivity. The system's effectiveness for CO_2 inverse modeling is tested using pseudo-observation data. The results of the sensitivity and inverse modeling tests demonstrate the potential usefulness of WRF-CO2 4DVar for regional CO_2 inversions.

1 Introduction

Quantification of surface-atmospheric carbon exchange is important for understanding the global carbon cycle (Peters et al., 2007). Both inventory based bottom-up and atmospheric inversion based top-down approaches have been widely used to investigate carbon sources and sinks. Most atmospheric CO_2 inversion methods are based on Bayes theorem, in which CO_2 flux is optimized by minimizing a quadratic form cost function consisting of background cost and observation cost. The minimization of the cost function can be achieved by analytical or variational approaches. Chevallier et al. (2005) provides a concise explanation of the differences between the two approaches.

Both analytical and variational inversions use a chemistry transport model (CTM) to relate CO_2 flux to atmospheric CO_2. From the perspective of an optimization system, atmospheric CO_2 forms the observation vector, and CO_2 flux forms the state

vector to be optimized. Central to all CO_2 inversion approaches is the Jacobian matrix which relates changes in flux to change in model-simulated atmospheric CO_2. For an inversion system with a $n \times 1$ state vector and a $m \times 1$ observation vector, its Jacobian matrix is a $m \times n$ matrix. Analytical inversions require the explicit construction of the Jacobian matrix, which can be carried out by either CTM (as the forward model) or its adjoint model. While a forward model calculates the Jacobian matrix by columns, an adjoint model calculates it by rows. The size of the state vector or observation vector determines the number of forward or adjoint model runs needed for constructing the Jacobian matrix. The practical limit imposed by the computational cost of the Jacobian matrix construction and the memory demand of matrix inversion often necessitate the aggregation of flux to reduce state vector size in analytical inversions, which leads to aggregation error (Bocquet, 2009; Kaminski et al., 2001; Turner and Jacob, 2015). In comparison, variational approaches do not require the Jacobian matrix to be explicitly constructed, instead they directly compute the product of the Jacobian with a forcing vector, which is the gradient vector used for optimizing the state vector.

A number of four dimensional variational (4DVar) assimilation systems have been developed and applied to global scale CO_2 inversions. The off-line transport model Parameterized Chemistry Tracer Model (PCTM) (Kawa et al., 2004) and its adjoint have been used for CO_2 inversions (Baker et al., 2010, 2006; Butler et al., 2010; Gurney et al., 2005). Chevallier et al. (2005) developed a 4DVar system based on the LMDZ model (Hourdin et al., 2006) to assimilate CO_2 observation data from Television Infrared Observation the Satellite Operational Vertical Sounder (TOVS). This system has also been used to invert surface CO_2 observation data (Chevallier, 2007; Chevallier et al., 2010) The TM5 4DVar system (Meirink et al., 2008), based on the TM5 global two-way nested transport model (Krol et al., 2005), is used in the CarbonTracker CO_2 data assimilation system (Peters et al., 2007) and is included in the TransCom satellite intercomparison experiment (Saito et al., 2011). TM5 4DVar has also been used to investigate total column CO_2 seasonal amplitude (Basu et al., 2011) and to assimilate the Greenhouse Gases Observing Satellite (GOSAT) observations (Basu et al., 2013). Another widely used inversion system is the GEOS-Chem 4DVar (Henze et al., 2007; Kopacz et al., 2009) with its CO_2 module updated by Nassar et al. (2010). GEOS-Chem 4DVar has been used to estimate CO_2 fluxes from the Tropospheric Emission Spectrometer (TES) and the GOSAT CO_2 observations (Nassar et al., 2011; Deng et al., 2014), and it is also part of JPL's (Jet Propulsion Laboratory) Carbon Monitoring System (Liu et al., 2014)

CO_2 inversions at regional scale have become an active research front in recent years, driven by the need to resolve biosphere-atmosphere carbon exchange at smaller scales (Gerbig et al., 2009), and by the need to address policy-relevant objectives, such as assessing emission reduction effectiveness (Ciais et al., 2014) and the impact of regional scale sources like wildland fire (French et al., 2011). A number of regional inversion systems have been developed and applied. For instance, GEOS-Chem 4DVar's nested simulation ability provides a means for regional inversions, such as its application for CH_4 inversion over North America (Wecht et al., 2014). The majority of regional inversions use analytical approaches and typically use a Lagrangian particle backward dispersion model (LPDM) to compute the required influence function. For instance, Gerbig et al. (2003) used an analytical approach to minimize the cost function and the STILT (Lin et al., 2003) model driven by assimilated meteorology

to calculate the influence function. In a later study, STILT driven by ECMWF meteorology is used to calculate the influence function to investigate the impacts of vertical mixing error (Gerbig et al., 2008). More recently, Lauvaux et al. (2012) also used an analytical solution for cost function minimization and LPDM (Uliasz, 1993) to compute the influence function. In another study, Pillai et al. (2012) used STILT driven by meteorology data from WRF to calculate the influence function for comparing Lagrangian and Eulerian models for regional CO_2 inversions. To improve accuracy, STILT has been coupled to WRF, in which the latter provides online meteorology to STILT to avoid interpolation error (Nehrkorn et al., 2010). More recently, Alden et al. (2016) investigated biopheric CO_2 flux in the Amazon using an analytical inversion approach (Yadav and Michalak, 2013) with influence function calculated by the STILT and Flexpart (Stohl et al., 2005) models. Also, Chan et al. (2016) applied a regional CO_2 inversion in Canada with both analytical and Markov chain Monte Carlo (MCMC) LPDM based approaches. Influence function is also calculated with the Flexpart model in this study.

While rising atmospheric CO_2 has been well documented by observational data, major uncertainties still exist in attributing it to specific processes. For instance, the two sets of terrestrial biosphere CO_2 flux databases in NASA's carbon monitoring system flux pilot project differ substantially (Ott et al., 2015). In order to better resolve the terrestrial biosphere's response to the rising CO_2, inverse modeling at the regional scale is a high research priority (Gerbig et al., 2009). Toward this end, a regional CO_2 inversion system with online meteorology, WRF-CO2 4DVar, was developed by modifying modifying the WRFDA and WRFPLUS system (v3.6) in an approach similar to that used for black carbon emission inversion by Guerrette and Henze (2015, 2017) (hereafter GH15/17). WRFDA is a meteorology data assimilation system, which includes a 4DVar assimilation system (Barker et al., 2012; Huang et al., 2009) and related adjoint and tangent linear models (WRFPLUS) (Zhang et al., 2013). Designed to improve weather forecasts, WRFDA 4DVar optimizes meteorological initial and boundary conditions by assimilating a variety of observational data. WRFPLUS was modified to include CO_2 related processes and the cost function was configured so that the state vector consists of CO_2 flux instead of meteorological fields. In developing WRFDA-Chem for black carbon inversion, GH15/17 excluded radiation, cumulus, and microphysics parameterization schemes from the tangent linear model and adjoint model because developing these procedures for black carbon would incur a large amount of new code development. In WRF-CO2 4DVar, CO_2 is a tracer, meaning its impacts on meteorology are ignored. This configuration allows inclusion of the full physics schemes in WRF-CO2 4DVar's tangent linear model and adjoint model with limited new code development (see Section 2.4.2). As transport model error is detrimental to 4DVar inversion accuracy (Fowler and Lawless, 2016; Gerbig et al., 2009), it is to use the full physics schemes in the tangent linear and adjoint models for WRF-CO2 4DVar. In addition, while GH15/17 excluded convective transport of chemistry species in WRFDA-Chem, the tangent linear and adjoint code for this process was developed for WRF-CO2 4DVar to reduce the vertical mixing error (see Section 2.4.4). Like GH15/17, an incremental optimization with Lanczos-CG was developed, as well as an L-BFGS-B based optimization. but we also implemented an L-BFGS-B based optimization.

In the WRF system, CO2 mixing ratio variations can impact the meteorology fields through the radiation scheme. This feedback is ignored in WRF-CO2 4DVar and instead CO2 is modeled as a passive tracer. WRF-CO2 4DVar is designed for regional

inversions with a short assimilation window (days to weeks). For such applications, the potential feedback of CO2 variation on the meteorology is insignificant for most cases. Including such impacts would require a large amount of new code development while offering very limited performance improvement. By ignoring the CO2 feedback, WRF-CO2 4DVar can use the full version of most WRF physics schemes in its tangent linear and adjoint models to minimize the linearization error (Tremolet, 2004).

Compared with offline regional inversion systems, WRF-CO2 4DVar has an advantage provided by the close one-way coupling between meteorological processes and chemistry transport. For example, adequately resolving CO2 vertical transport in high resolution regional simulations is crucial and vertical motions in the atmosphere exhibit significant temporal variability. Grell et al. (2004) shows that less than 40% of the total vertical velocity variability in a 3 km resolution simulation is captured by 1-hour output interval. He estimate that the meteorological output interval must be less than 10 minutes in order to capture more than 85% of the variability in cloud resolving simulations. In WRF-CO2 4DVar, CO2 transport runs at the same time step as the meteorology, avoiding the problems facing its offline counterparts.

The remainder of this paper is organized as follows: Section 2 details the implementation of the two variational optimization schemes for cost function minimization, and the modification to the tangent linear and adjoint models. Section 3 examines the accuracy of sensitivity calculated by the tangent linear and adjoint models, and the system's effectiveness in inverse modeling. Finally, a summary and outlook are presented in Section 4.

2 Method

This section describes the WRF-CO2 4DVar cost function configuration and the associated minimization schemes, followed by a description of the forward, tangent linear, and adjoint models.

2.1 Cost function configuration

WRF-CO2 4DVar is designed to optimize CO_2 flux by assimilating CO_2 observational data into an atmospheric chemistry transport model. CO_2 flux is optimized through use of a linear scaling factor:

$$E = k_{co2}\widetilde{E} \tag{1}$$

Where $\widetilde{E}$ is the CO_2 emission read from emission files, k_{co2} is the emission scaling factor, and E is the effective CO_2 flux. It is the effective flux that is used in WRF-Chem's emission driver to update CO_2 mixing ratio (q_{co2}). The emission scaling factor k_{co2}, its tangent linear variable g_k_{co2}, and its adjoint variable a_k_{co2} are used in calculating model sensitivity and minimizing the cost function defined in Eq. (2). The readers can find a list of the notations used in this article in Table 1. Throughout the paper, bold face lower case characters represent vectors and bold face upper case characters represent matrices.

The cost function $J(\mathbf{x})$ of WRF-CO2 4DVar follows the Bayes framework widely used in atmospheric chemistry and numerical weather prediction (NWP) data assimilations:

$$J(\mathbf{x}) = J_b(\mathbf{x}) + J_o(\mathbf{x}) \tag{2}$$

where the background cost function $J_b(\mathbf{x})$ is defined as

$$J_b(\mathbf{x}) = \frac{1}{2}(\mathbf{x}^n - \mathbf{x}^b)^T \mathbf{B}^{-1}(\mathbf{x}^n - \mathbf{x}^b) \tag{3}$$

and the observation cost function $J_o(\mathbf{x})$ is defined as

$$J_o(\mathbf{x}) = \frac{1}{2}\sum_{k=1}^{K}\{H[M(\mathbf{x}^n)] - \mathbf{y}\}^T \mathbf{R}^{-1}\{H[M(\mathbf{x}^n)] - \mathbf{y}_k\} \tag{4}$$

In Eqs. (3-4), the superscript n indicates that $\mathbf{x}^n$ is the optimized state vector at the n$^{\text{th}}$ iteration.

Like other data assimilation systems, WRF-CO2 4DVar is essentially an optimization scheme. Its state vector $\mathbf{x}$ consists of the emission scaling factors k_{co2}. The summation K in Eq. (4) indicates the entire assimilation time period is evenly split into K observation windows during which observational data are ingested into the assimilation system.

Two optimization schemes are implemented in WRF-CO2 4DVar to minimize the cost function. The first scheme uses a limited memory BFGS minimization algorithm (L-BFGS-B) (Byrd et al., 1995) and the second uses the Lanczos version of the conjugate gradient (Lanczos-CG) (Lanczos, 1950) minimization algorithm. Both schemes are iterative processes, and they call on WRF-CO2 4DVar model components (the forward, tangent linear, and adjoint models) to calculate the model sensitivity $\partial q_{co2}/\partial k_{co2}$ between the iterations. The two optimization schemes are described in Section 2.2 and 2.3, respectively, and the three model components are described in Section 2.4.

2.2 L-BFGS-B optimization

L-BFGS-B (Byrd et al., 1995) is a quasi-Newton method for nonlinear optimization with bound constraints. L-BFGS-B has been used in a number of atmospheric chemistry inverse modeling systems, including the GEOS-Chem adjoint model system (Henze et al., 2007) and the TM5 4DVar system (Meirink et al., 2008). The diagram in Fig. 1 demonstrates the steps involved in the L-BFGS-B based optimization scheme. The scheme is an iterative process which searches for the optimized k_{co2} by minimizing the cost function defined in Eq. (2-4). Between its iterations, the minimization algorithm L-BFGS-B requires the values of the cost function and its gradient, which are supplied by the forward model and the adjoint model as indicated in Fig. 1.

The calculation of the cost function is carried out based on Eq. (2-4). Starting with the prior estimate of k_{co2}, the forward model run generates the CO_2 mixing ratio q_{co2}, which is transformed from the WRF model space to the observation space by the forward observation operator H. This results in the $H(M(\mathbf{x}^n))$ term in Eq. (4), which is then paired with the observation

vector $\mathbf{y}_k$ to calculate the innovation vector $\mathbf{d}_k = H(M(\mathbf{x}^n)) - \mathbf{y}_k$. Next, the innovation vector and observation error covariance $\mathbf{R}$ are used to calculate the observation cost function $J_o(\mathbf{x})$ as expressed in Eq. (4). Finally, the background cost function $J_b(\mathbf{x})$ is calculated according to Eq. (3), and combined with the observation cost function $J_o(\mathbf{x})$ to form the total cost function $J(\mathbf{x})$ according to Eq. (2).

L-BFGS-B requires the values of the cost function $J(\mathbf{x})$ and its gradient $\nabla J(\mathbf{x})$ in searching for the optimized k_{co2}. The gradient is calculated using Eq. (5).

$$\nabla J(\mathbf{x}) = \sum_{k=1}^{K} \widetilde{M}^T \widetilde{H}^T R^{-1} \{H[M(\mathbf{x}^n) - \mathbf{y}_k]\} + B^{-1}(\mathbf{x}^n - \mathbf{x}^b) \tag{5}$$

The first term on the right hand side of Eq. (5) is the observation gradient and the second is the background gradient. The observation gradient is calculated in two steps: (1) The innovation vector is scaled by $\mathbf{R}^{-1}$ and transformed to the WRF model space by the adjoint observation operator, resulting in $\widetilde{H}^T \mathbf{R}^{-1}(H(M(\mathbf{x}^n)) - \mathbf{y}_k)$, which is the adjoint forcing. (2) The adjoint forcing is ingested by the WRF-CO2 adjoint model during its backward (in time) integration, which yields the observation gradient. Supplied with the values of the cost function and gradient, the L-BFGS-B algorithm finds a new value of k_{co2}, which is used for the next iteration. The iterative optimization process continues until a given convergence criterion is met. The L-BFGS-B based optimization in WRF-CO2 4DVar is implemented based on the Fortran code of Algorithm 788 version Lbfgsb.2.1 (Zhu et al., 1997). Version Lbfgsb.3.0 (Luis Morales and Nocedal, 2011) will be implemented in the next model update.

2.3 Incremental optimization

The second optimization scheme implemented for WRF-CO2 4DVar was the incremental approach commonly used in NWP data assimilation systems, including ECWMF 4DVar (Rabier et al., 2000) and WRFDA (Barker et al., 2012). A major difference between the L-BFGS-B based optimization and the incremental optimization is that the former optimizes for the state vector while the latter optimizes for the state vector analysis increment. The incremental assimilation scheme uses a linear approximation to transform the observation cost function from what is defined in Eq. (4) to Eq. (6):

$$J_o(\mathbf{x}) = \frac{1}{2} \sum_{k=1}^{K} \{H[M(\mathbf{x}^{n-1})] - \mathbf{y}_k + \widetilde{H}[\widetilde{M}(\mathbf{x}^n - \mathbf{x}^{n-1})]\}^T \mathbf{R}^{-1} \{H[M(\mathbf{x}^{n-1})] - \mathbf{y}_k + \widetilde{H}[\widetilde{M}(\mathbf{x}^n - \mathbf{x}^{n-1})]\} \tag{6}$$

Compared to Eq. (4), Eq. (6) approximates the innovation vector by a sum of two parts. The first part, $H(M(\mathbf{x}^{n-1})) - \mathbf{y}_k$, is the innovation vector from the previous iteration. The second part, $\widetilde{H}(\widetilde{M}(\mathbf{x}^n - \mathbf{x}^{n-1}))$, is the state vector analysis increment $(\mathbf{x}^n - \mathbf{x}^{n-1})$ transformed by the tangent linear model $\widetilde{M}$ and tangent linear observation operator $\widetilde{H}$. With the linear

approximation of the cost function the gradient is calculated by

$$\nabla J(\mathbf{x}) = \sum_{k=1}^{K} \widetilde{M}^T \widetilde{H}^T \mathbf{R}^{-1}\{H[M(\mathbf{x}^{n-1}) - \mathbf{y}_k]\} + \mathbf{B}^{-1}(\mathbf{x}^{n-1} - \mathbf{x}^b) + \sum_{k=1}^{K} \widetilde{M}^T \widetilde{H}^T \mathbf{R}^{-1}\{\widetilde{H}[\widetilde{M}(\mathbf{x}^n - \mathbf{x}^{n-1})]\} + \mathbf{B}^{-1}(\mathbf{x}^n - \mathbf{x}^{n-1}) \quad (7)$$

In WRF-CO2 4DVar, the incremental optimization is implemented as a double loop in which the outer loop calculates the first and second items on the right hand side of Eq. (7), while the inner loop calculates the third and fourth items. The superscript $n-1$ indicates that $\mathbf{x}^{n-1}$ is the optimized state vector in the last outer loop, and superscript n indicates that $\mathbf{x}^n$ is the optimzed state vector in the inner loop. The outer loop first calls the forward model M and adjoint model $\widetilde{M}^T$ to calculate $\widetilde{M}^T \widetilde{H}^T R^{-1}(H(M(\mathbf{x}^{n-1}) - \mathbf{y}_k))$ and $B^{-1}(\mathbf{x}^{n-1} - \mathbf{x}^b)$, which remain unchanged during the subsequent inner loop calculation. The analysis increment $(\mathbf{x}^n - \mathbf{x}^{n-1})$ is optimized in the inner loop, which calls the tangent linear and adjoint models to calculate the third and fourth items of Eq. (7). Inner loop calculation is carried out by Lanczos-CG (Lanczos, 1950), which can optionally estimate eigenvalues of the cost function Hessian matrix ($\nabla^2 J(\mathbf{x})$). The diagram in Fig. 2 shows the structure of the Lanczos-CG based incremental optimization implemented in WRF-CO2 4DVar.

2.4 Forward, tangent linear, and adjoint models

WRFPLUS consists of three model components: the WRF model, its tangent linear model, and its adjoint model (Barker et al., 2012; Huang et al., 2009). The three models are used by WRFDA to optimize the initial meteorological condition in order to improve numerical weather prediction. Unlike WRFDA, WRF-CO2 4DVar is designed to optimize CO_2 flux, instead of the meteorological initial and boundary conditions. This difference means CO_2 related processes are needed in WRF-CO2 4DVar's model components. To include the CO_2 related processes, WRF-Chem was used to replace WRF as the forward model. Then, a thorough variable dependence analysis was conducted to determine how to modify the tangent linear and adjoint model in order keep them consistent with WRF-Chem (the forward model).

2.4.1 Forward model

WRF-Chem replaced WRF as the forward model component of WRF-CO2 4DVar. As an atmospheric chemistry extension of WRF, WRF-Chem includes chemistry, deposition, photolysis, advection, diffusion, and convective transport of chemistry species (Grell et al., 2005). These processes are included in different modules of WRF-Chem: ARW (Advanced Research WRF) dynamical core, physics driver, and chemistry driver. The GHG (Greenhouse Gas) tracer option of WRF-Chem was used but with the CO and CH_4 removed, leaving only CO_2 related procedures. In the emission driver, CarbonTracker 2016 version (Peters et al., 2007) replaces the online biogenic CO_2 model Vegetation Photosynthesis and Respiration Model (VPRM) (Mahadevan et al., 2008). This change is made because WRF-CO2 4DVar optimizes for CO_2 flux instead of online emission model parameters.

2.4.2 Variable dependence analysis

The tangent linear and adjoint models of WRFPLUS need to be modified to include the CO2 related processes so that they will be consistent with the forward model. The results of the variable dependence analysis is summarized in Table 2, which groups WRF-Chem processes into three categories regarding CO_2 tracer transport. The first category includes the chemistry processes that do not apply to CO_2, including gas and aqueous phase chemistry, dry and wet deposition, and photolysis. These processes are simply excluded from the forward, tangent linear, and adjoint models in WRF-CO2 4DVar.

The second category is comprised of the physical parameterizations that do not provide CO_2 tendency, but provide meteorological tendency. This category includes radiation, surface, cumulus, and microphysics parameterizations. While the full physics schemes of surface, cumulus, planetary boundary layer (PBL), and microphysics are used in the forward model of WRFPLUS, simplified versions of these schemes are used in its tangent linear and adjoint models. In addition, WRFPLUS uses full radiation schemes (longwave and shortwave) in its forward model, but it excludes radiation schemes from its tangent linear model and adjoint model. The differences in the physical parameterizations between the forward model and tangent linear/adjoint models in a 4DVar system is a source of linearization error. For instance, Tremolet (2004) found linearization error in ECMWF 4DVar larger than expected and recommended more accurate linear physics for higher resolution 4DVar systems. Because WRF-CO2 4DVar ignores the impacts of CO_2 mixing ratio variation on the meteorological fields, no tangent linear and adjoint variables for meteorological fields are needed in its tangent linear model and adjoint model. Since this second category of processes are not directly involved in CO_2 transport, there is no need for their tangent linear and adjoint procedures in WRF-CO2 4DVar. In WRFPLUS's tangent linear model, the tangent linear code of the simplified versions of the cumulus, surface, and microphysics schemes, were removed and replaced with their corresponding full schemes as used in the forward model. In WRFPLUS's adjoint model, the forward sweep updates the state variables and local variables just as in the forward model, but it also stores these variables' values for the subsequent backward sweep, which updates the adjoint variables of the state variables. The simplified versions of the cumulus, surface, and microphysics schemes used in the forward sweep of WRFPLUS's adjoint model, were removed and replaced with the full schemes used in the forward model. Since these processes do not directly modify CO_2 mixing ratio, their corresponding adjoint code wes removed from the backward sweep of the adjoint model, as indicted by the 'X' in Table 2.

The third category includes advection, diffusion, emission, and turbulence mixing in PBL, along with convective transport of CO_2. Because these processes directly modify CO_2 mixing ratio, their tangent linear code and adjoint code are needed for WRF-CO2 4DVar. The modifications made for advection and diffusion are described in Section 2.4.3, and those for emission, turbulent mixing in PBL, and convective transport of CO_2 are detailed in Section 2.4.4.

2.4.3 Advection and diffusion of CO2

WRF includes the advection and diffusion of inert tracers along with other scalars in its ARW dynamical core. The tangent linear and adjoint code of these processes has been implemented in WRFPLUS. It should be noted that the variables for these inert tracers are part of WRF, instead of WRF-Chem. WRF-Chem uses a separate array for its chemistry species. Since WRF was replaced with WRF-Chem as the forward model in WRF-CO2 4DVar, the CO_2 mixing ratios are included in the chemistry array. In the GHG option of WRF-Chem used for WRF-CO2 4DVar, CO_2 from different sources (anthropogenic, biogenic, biomass burning, and oceanic) are represented by separate variables in the chemistry array. Following the treatment for the inert tracers in WRFPLUS, subroutines solve_em_tl and solve_em_ad were modified to add the tangent linear and adjoint code for the advection and diffusion of the chem array. The modifications made include adding calls to the procedures that calculate advection and diffusion tendencies, updating the chemistry array with the tendencies and boundary conditions, and addressing the Message Passing Interface (MPI) communications. The new upgrade to WRFPLUS described in (Zhang et al., 2013) greatly expedited this part of development for WRF-CO2 4DVar. The 'Add' in Table 2 for advection and diffusion emphasizes that their tangent linear and adjoint code are added to WRF-CO2 4DVar based on the existing WRFPLUS code without substantial new code development.

2.4.4 Vertical mixing of CO_2 in PBL and convective transport

An accurate representation of vertical mixing is important for inversion accuracy, because misrepresentation causes transport error, which manifests itself in the innovation vector and causes error in posterior estimation (Fowler and Lawless, 2016). For instance, Stephens et al. (2007) pointed out that global chemistry transport model error in vertical mixing and boundary layer thickness could cause significant overestimation of northern terrestrial carbon uptake. A comparison of four global models found that model transport uncertainty exceeds the target requirement for A-SCOPE mission of 0.02 Pg C yr^{-1} per 10^6 km^2 (Houweling et al., 2010). In addition, Jiang et al. (2008) reported that convective flux is likely underestimated in boreal winter and spring based on simulated upper tropospheric CO_2 from 2000 to 2004 using three chemistry transport models.

In WRF-Chem, vertical mixing of chemical species is treated in three separate parts: in the vertical diffusion (subgrid scale filter) in the dynamical core, in the PBL scheme in the physics driver, and within convective transport in the chemistry driver. The subgrid scale filter in the dynamical core treats both horizontal and vertical diffusions, but vertical diffusion is turned off if a PBL scheme is used. While all PBL schemes implemented in WRF-Chem treat the vertical turbulent mixing of temperature and moisture, only the ACM2 PBL scheme also treats chemistry species (Pleim, 2007). The ACM2 scheme was chosen for in WRF-CO2 4DVar so that CO_2 vertical mixing is treated by the PBL parameterization. Convective transport of chemistry species in WRF-Chem is not treated by the cumulus scheme in the physics driver, but by a separate convective transport module (module_ctrans_grell) in the chemistry driver (Grell et al., 2004).

Because the ACM2 PBL and chemistry convective transport are not included in WRFPLUS, their tangent linear and adjoint code were developed for WRF-CO2 4DVar. First the automatic differentiation tool TAPENADE (Hascoet and Pascual, 2013) was used to generate the tangent linear and adjoint code based on the forward code: module_bl_acm for the ACM2 PBL and module_ctrans_grell for the chemistry convective transport. Then the TAPENADE generated code was manually modified to remove redundancy and unnecessary loops. It should be pointed out that these code developments were made significantly simpler because the meteorological state variables are merely passive variables in the tangent linear and adjoint code. For instance, to calculate the moist static energy and environmental values on cloud levels, the chemistry convective transport code (module_ctrans_grell) in the chemistry driver calls a number of subroutines in the cumulus parameterization code in the physics driver. Because these subroutines in cumulus parameterization only involve meteorology state variables and not the chemistry array, no tangent linear or adjoint code is needed for them in WRF-CO2 4DVar.

3 Results

This section presents an accuracy assessment of the newly developed WRF-CO2 4DVar system. First the simulation model setup is described, then the sensitivity tests and inverse modeling experiments presented.

3.1 Model setup

WRF-CO2 4DVar is setup with a domain covering the continental United States with 48 km $\times$ 48 km grid spacing and 50 vertical levels (Fig 3.). The domain dimension is 110 points in east-west and 66 points in north-south direction. Model configuration includes: Rapid Radiative Transfer Model (RRTM) longwave radiation (Mlawer et al., 1997), Goddard shortwave radiation (Chou and Suarez, 1999), Pleim surface layer (Pleim, 2006), Pleim-Xiu land surface model (Pleim and Xiu, 2003), ACM2 PBL (Pleim, 2007), Grell-Freitas cumulus (Grell and Freitas, 2014), and Thompson microphysics (Thompson et al., 2008). Positive-definite transport is applied to the transport of scalars and CO_2.

CO_2 fluxes used for the simulations are from the CarbonTracker 2016 version (hereafter CT2016) (Peters et al., 2007). These fluxes are the optimized surface fluxes at a 3-hour interval and at 1×1 degree spatial resolution. The four individual CO_2 fluxes (biosphere, fossil fuel, fire, and ocean) are spatially interpolated to the WRF grid, and saved in chemistry input files. In the following sensivitity tests and inverse experiments, the emission scaling facotr k_{co2} is applied only to the biosphere flux. Daily mean biosphere fluxes are calculated as the arithmatic mean of the 3-hourly CT2016 fluxes at each surface grid cell, and the scaling factor k_{co2} is applied as in Eq. (1). The daily mean biosphere flux used for the 24 hour simulation is shown in Figure 4. The model configuration and emission data used are summarized in Table 3.

Model simulations span 24 hours from 00 UTC 02 June to 00 UTC 03 June, 2011. Meteorological initial and lateral boundary conditions are prepared using the NCEP Climate Forecast System Version 2 (CFSv2) 1×1 degree 6-hourly products (Saha

et al., 2014). CO_2 initial and lateral boundary conditions are from the CT2016 global 3×2 degree CO_2 mole fraction. A method similar to PREP-CHEM-SRC (Freitas et al., 2010) was used to horizontally and vertically interpolate CT2016 mole fraction data to the WRF grid.

First, the forward model (WRF-Chem) was run for 24 hours with the CO_2 emission as described in the last section. Trajectory files that contain model state variables including both meteorology and CO_2 mixing ratio are saved at model dynamical time step intervals (120 seconds). These files are required for the subsequent tangent linear and adjoint model runs. Figure 4 shows the instantaneous values of Sea Level Pressure (SLP) and horizontal wind at the model's lowest vertical level at each 6 hours. The figure shows that a high pressure system was located off the west coast, causing a northerly surface wind off southern California, and a westerly wind for most of the Pacific Northwest. A low pressure system intensified over Montana and North Dakota during the 24 hours, causing a strong southerly wind over the Midwest. In the northeast, as a low pressure system moved eastward out of the domain, the surface wind shifted from southwesterly to westerly.

In the model setup, the initial and boundary meteorological conditions are generated by downscaling the CFSv2 data. Downscaling coarse resolution global reanalysis data could lead to poor WRF performance. Although this potential problem is not a concern for the present pseudo data based inversion experiments, it must be properly treated in the future application with true observation data. Error in the initial condition will lead to erroneous emission source attribution, especially for inversions with short assimilation window.

In order to be useful for applications which employ real observational data, WRF-CO2 4DVar requires accurate simulation of the meteorological fields by the forward model, in addition to accurate tangent linear and adjoint models. Because transport error can only be partially accounted for in the 4DVar system through the observation error variance, it is imperative to minimize errors due to inaccurate simulation of meteorological processes as much as possible. Although the present paper uses pseudo-observation data (which have zero transport error by definition) in its inversion experiments, future applications with true observational data will require vigorous evaluation of the model simulated meteorology and associated transport error. In the following, the forward model simulated horizontal winds at the surface and 500 hPa constant pressure surface are evaluated using in-situ measurements from weather stations and radiosondes.

For the surface level, WRF simulated 10m winds are compared against surface weather station measurements archived in the NOAA Integrate Surface Dataset (Smith et al., 2011). Hourly surface wind measurements from more than 2,000 stations within the WRF domain are used for the evaluation. Comparisons of wind speed and wind direction are carried out at the top of each hour during the 24 hour simulation period starting at 00:00 UTC 02 June 2011. Excluding missing observations, this results in 31,745 valid data pairs, which are summarized in the histograms of Fig. 6. RMSE for the hourly wind speed is 2.16 m s^{-1} and the mean difference in the hourly wind direction is 29.4°.

For the upper level, WRF simulated 500 hPa horizontal winds were compared against radiosonde measurements from 90 stations obtained from the NOAA/ESRL radiosonde database (https://ruc.noaa.gov/raobs/). Since most stations release balloon at 00:00 and 12:00 UTC, WRF winds were compared against the radiosonde measurements at a 12 hour interval during the 24 hour simulation period. The results are shown in Figure 7: RMSE of wind speed is 2.54, 4.0, and 5.11 m s^{-1}, at 2 June 00:00 UTC, 2 June 12:00 UTC, and 3 June 00:00 UTC, respectively. Wind direction difference between WRF and radiosonde is 11.5°, 16.4°, and 19.1° at the three times. Locations of the weather stations and radiosonde sites used in the evaluations can be found in the supplement document.

The above-described evaluations using in-situ measurements indicate that the meteorological simulation is of adequate accuracy for the pseudo observation based inverse modeling tests conducted in this paper. Future applications with true observational data will need to quantify the simulation error in the 4DVar system.

3.2 Accuracy of tangent linear and adjoint sensitivities

Next,the accuracy of the newly developed tangent linear and adjoint models wereby comparing their sensitivity calculations against finite difference sensitivity calculated by the forward model. Grid cells involved in the sensitivity calculations are shown in Fig. 3, in which the 35 blue stars are the source cells, and the 20 red triangles are 20 tower sites where the receptors are placed. All the 35 sources are placed at the grid's bottom vertical level. Receptors are placed at the 1st, 5th, and 10th vertical level at each of the 20 tower sites, resulting in 60 receptor cells.

A tangent linear model run for a grid cell will calculate the tangent linear sensitivity $\partial \mathbf{q_{co2}}/\partial k_{co2}$, which approximates a column vector of the forward model's Jacobian matrix and quantifies the influence of the cell's emission change on CO_2 mixing ratio of its receptor cells downwind. In comparison, an adjoint model run for a grid cell will calculate adjoint sensitivity $\partial q_{co2}/\partial \mathbf{k_{co2}}$, which approximates a row vector of the forward model's Jacobian matrix and quantifies the influence on the cell's CO_2 mixing ratio by its source cells upwind. Because k_{co2} multiplies emission in Eq. (1), the magnitude of the sensitivity is determined by both the magnitude of emission and meteorological transport.

To calculate tangent linear sensitivity at a grid cell, g_k_{co2} is set to unity at the cell and zero at all other cells at the start of a tangent linear model run. Upon completion, the values of $\mathbf{g\_q_{co2}}$ are the tangent linear sensitivities $\partial \mathbf{q_{co2}}/\partial k_{co2}$. To calculate adjoint sensitivity at a cell, an adjoint model run starts with a_q_{co2} set to unity at the cell and zero at all others, and the values of $\mathbf{a\_k_{co2}}$ at the end of the simulation are the adjoint sensitivities. The adjoint model running in this mode is analogous to using a Lagrangian particle transport model in backward trajectory mode to compute the footprint of a receptor, such as shown in Fig 4. of Gerbig et al. (2008).

The tangent linear sensitivity is first compared against the finite difference sensitivity. After confirming the accuracy of the tangent linear model, the adjoint sensitivity is compared against the tangent linear sensitivity.

Finite difference sensitivities are calculated using the two-sided formula (Eq. (8)).

$$\frac{\partial f}{\partial x} = \frac{f(x+\Delta x) - f(x-\Delta x)}{2\Delta x} \tag{8}$$

The magnitude of Δx used in Eq. (8) is determined by comparing the result from a range of different values. The finite sensitivities were calculated at the 35 sites using Δx set to 0.01, 0.1, and 1.0, and the results show that the magnitude of all differences is less than 10^{-10} (results not shown) because WRF-CO_2 is largely linear. For all subsequent calculations, $\Delta x = 0.1$ is used for Eq. (8).

Sinceboth finite difference and tangent linear sensitivities form columns of the Jacobian matrix, their values can be compared cell by cell for all receptor cells for a given site. Figure 8 shows the comparison between the finite difference and tangent linear sensitivities at 9 of the 35 source cells. The dark straight lines in the figures are the 1:1 line. The maximum and minimum of the difference between finite difference and tangent linear sensitivities are given for each source cell. Results at the rest of the sources are similar (not shown). All differences are less than 10^{-10}, confirming that the tangent linear model is accurate.

The adjoint model is next evaluated by comparing adjoint sensitivities against the tangent linear sensitivities. Because finite difference sensitivities form columns of the Jacobian matrix while adjoint sensitivities form rows of the Jacobian matrix, they can only be compared at the intersections of the rows and columns of the Jacobian matrix, meaning there are 2160 (35×60) pairs of comparison. We organized these 2160 pairs into three groups based on the vertical levels a receptor is placed at and the result is shown in Fig. 9. The minimum and maximum value of the difference between tangent linear and adjoint sensitivities in all three groups are no greater than 10^{-6}, indicating that the adjoint model is accurate.

3.3 Spatial patterns of adjoint sensitivities

Adjoint sensitivity $q_{co2}/\mathbf{k}_{co2}$ quantifies how q_{co2} of a given receptor is impacted by the emission scaling factor of all surface cells. It is similar to the receptor footprint typically calculated using LPDM, such as Fig. 4 of Gerbig et al. (2008) and Fig. 1 of Alden et al. (2016). But $q_{co2}/\mathbf{k}_{co2}$ differs from footprint in that the former contains the combined impact of tracer transport and emission magnitude, while the latter is determined by tracer transport alone. The spatial patterns of the adjoint sensitivity was examined to discern the impacts of tracer transport. Figure 10 shows $q_{co2}/\mathbf{k}_{co2}$ of Centerville, Iowa (top row) and WLEF, Wisconsin (bottom row). At each tower site, $q_{co2}/\mathbf{k}_{co2}$ of receptor placed at the 1st and 10th vertical levels are plotted.

The adjoint sensitivities of the Centerville tower site indicate its q_{co2} results primarily from surface flux located immediately south of the site. This pattern agrees with the fact that low level wind during the simulation period is predominantly southernly, tranporting tracers northward. There is also a marked difference in the adjoint sensitivity of the same tower site when the receptor is placed at a different height. The figure in the top left panel shows that the highest magnitude of $q_{co2}/\mathbf{k}_{co2}$ is closest

to the tower itself, indicating a large impact from local flux. In comparison, when the receptor is placed at the 10^{th} vertical level, the peak magnitude of its adjoint sensitivity is a much farther distance southward, and it features much wider spread, indicating transport of flux distant from that receptor is dominant. Results from WLEF shows the adjoint sensitivity are located to the southeast of the site, matching the southeasterly wind patterns around Wisconsin during the simulation period. There are also clear difference between the receptors at the different vertical levels. Results from other sites all show similar pattern of impacts of transport and receptor placement height (not shown).

To provide a comparative view of the source-receptor relations, backward trajectories of particles released from the Centerville and WLEF sites were also calculated using the Lagrangian model HYSPLIT (Stein et al., 2015). WRF-CO2 forward model simulated meteorology saved at 1-hour intervals is used to drive the HYSPLIT trajectory calculations. Two sets of simulations were carried out for each of the two tower sites: particles were released from the height approximates the first vertical level in WRF in the first set, and from the tenth level in the second. Each set of simulation consists of 300 particles, and their starting locations were uniformly distributed within a 48x48 km grid box corresponding with the WRF grid spacing. The HYSPLIT backward trajectory simulation results wre plotted in Fig. 11. To avoid cluttering the figures, the trajectories are plotted using only 60 out the 300 particles released in each case. The backward trajectories demonstrate similar spatial patterns as the adjoint sensitivities (Fig. 10). On the other hand, there are discernible differences between the two, which can be attributed to that representation of some tracer transport processes in HYSPLIT that are different from WRF, especially diffusion and convective transport.

3.4 Inverse modeling test

After confirming the validity of the tangent linear and adjoint models, the effectiveness of WRF-CO2 4DVAR in inverse modeling experiments was tested. Pseudo-observation data generated by the forward model run were used in these inverse modeling experiments, which start with prescribed prior values for the emission scaling factors and seek to recover their true values. To generate pseudo-observation data, the forward model ran for 24 hours with emission scaling factor set to unity at all surface grid points, saving CO_2 mixing ratio (q_{co2}) every 4 hours. This generated a set of six pseudo-observation files, each of which include the instantaneous q_{co2} at the model's first 30 vertical levels starting from the bottom level at each grid point. Given the simulation domain dimension, each individual observation file contains $110 \times 60 \times 30$ data entries.

Inverse modeling experiments were conducted for two cases of prior k_{co2}. In the first case, the prior emission scaling factor overestimates the true values by 50% ($k_{co2} = 1.5$ at all cells). In the second case, the prior emission scaling factor is randomly distributed between 0.5 and 1.5. Figure 12 shows the two experiment cases as scatter plots between the true biosphere CO_2 and its background value (the prior).

Both L-BFGS-B and incremental optimization (Lanczos-CG) are applied to the two cases, giving four inverse modeling experiments in total. In all four experiments, background error covariance is set to infinity ($\mathbf{B^{-1}} = \mathbf{0}$) and equal weights are

assigned to all observations ($\mathbf{R}$ set to identity matrix). This configuration is equivalent of (1) the setting total cost function to the observation cost function, and (2) setting the gradient to the observation gradient. It should be pointed out that this is an unrealistically simplified treatment of $\mathbf{B}$ and $\mathbf{R}$, used here for the sole purpose of testing the WRF-CO2 4DVar system with error-free pseudo-observations.

Because the pseudo-observation data are of q_{co2} at the forward model's grid points, the mapping between model space and observation space is trivial: the observation operator, tangent linear observation operator, and adjoint observation operator are all set to the identity matrix. Again, it should be noted that application of real observation data will require development of observation operators and their tagent linear and adjoint counterparts.

The results from inverse modeling experiments with Case 1 prior are shown in Fig. 13 and 14. Figure 10 shows the iterative reduction of the cost function $J(\mathbf{x})$, gradient norm $\|\nabla J(\mathbf{x})\|$, and RMSE. The iteration number for Lanczos-CG is all from its inner loop, and only one outer loop is used. The figures show both L-BFGS-B and Lanczos-CG reduce the cost function monotonically. In about the first 10 iterations, the cost function reduction is more or less similar for the two optimization schemes, but Lanczos-CG starts to gradually outperform L-BFGS-B after. In gradient norm reduction, both schemes feature periodic oscillations embedded in the large scale downward trend. By comparison, Lanczos-CG has a smaller magnitude oscillation and steeper downward trend than L-BFGS-B. It should be noted while L-BFGS-B calculates cost function and its gradient in each iteration, Lanzcos-CG only approximates these values in its inner loop. The cost function and gradient norm from Lanczos-CG shown in Fig. 10 are calculated by extra calls to the forward and adjoint models in each inner iteration, which doubles the computation cost and is not needed in practice. Figure 10(c) shows that both optimization schemes reduce RMSE of daily biosphere flux monotonically, and Lanczos-CG achieves better reduction after about the first 10 iterations. Figure 12 shows the snapshots of the optimized daily mean biosphere flux (obtained as the product of the prior flux and the optimized scaling factor) at a selected set of iterations. These figures depict the iterative process of priors converging to the true soluction.

The results of inverse modeling experiments using Case 2 prior are shown in Fig. 15 and 16. The reductions of $J(\mathbf{x})$, $\|\nabla J(\mathbf{x})\|$, and RMSE are similar to Case 1 in that Lanczos-CG substantially outperforms L-BFGS-G after about first 10 iterations. Table 5 summarizes the results from all four inverse modeling experiments described above. It must be pointed out that these inverse modeling results are obtained from a highly unphysical setup, and they are not the expected level of performance (in terms of cost function and RMSE reduction) that would be obtained in a real inversion.

4 Summary and outlook

WRF-CO2 4DVar was developed as a data assimilation system designed to constrain surface CO_2 flux by combining an online atmospheric chemistry transport model and observation data in a Bayesian framework. Two optimization schemes were implemented for cost function minimization. The first is based on L-BFGS-B and the second is an incremental optimization using

Lanczos-CG. The cost function and its gradient required by the optimization schemes are calculated by WRF-CO2 4DVar's three component models: forward, tangent linear, and adjoint model, all developed on top of the WRFPLUS system. While WRFPLUS's forward model is WRF, WRF-Chem was used as WRF-CO2 4DVar's forward model to include CO_2 in the system, and the tangent linear and adjoint models were modified to keep their consistency with the forward model. Like most other CO_2 inverse modeling systems, WRF-4DVar ignores the possible impacts of atmospheric CO_2 variation on the meteorology. This simplification enables the use of the same full physical parameterizations in the forward, tangent linear, and adjoint model. This configuration reduces linearization error while allowing the WRF system's large number of physical parameterizations to be used in WRF-CO2 4DVar without requiring a large amount of new code development.

WRF-CO2 4DVar's tangent linear and adjoint models were tested by comparing their sensitivities' spatial patterns with the dominant wind patterns. The results make physical sense given the meteorological transport. The accuracy of tangent linear and adjoint models were evaluated by comparing their sensitivity against finite difference sensitivity calculated by the forward model. The results show that both tangent linear and adjoint sensitivities agree well with finite difference sensitivity. Finally, the system was tested in inverse modeling with pseudo-observation data, and the results show that both optimization schemes successfully recovered the true values with reasonable accuracy and computation cost.

While Lanczos-CG performs better than L-BFGS-B in the inverse modeling tests, it must be pointed out that the tests are very limited. Although a comprehensive comparison between the two optimization schemes is beyond the scope of the present paper, it is important to point out some of their differences as implemented in WRF-CO2 4DVar. First, the Lanczos-CG calls the tangent linear model in each inner loop iteration, while L-BFGS-B calls the forward model. For a tracer transport system like WRF-CO2 4DVar, the tangent linear model can skip some of the costly physics parameterizations, such as the radiation scheme. This difference means that typically the tangent linear model is faster than the forward model, and as a result Lanczos-CG runs faster than L-BFGS-B. In our inversion modeling experiments (24-hour simulation with $\Delta t = 120$ seconds, 30 processor core), it takes about 10 minutes walltime to complete one inner loop of Lanczos-CG. L-BFGS-B takes about 10% more walltime to complete one iteration.

Second, provided with the cost function and its gradient, each iteration of L-BFGS-B calculates an updated state vector from its previous iteration. In WRF-CO2 4DVar, this calculation is carried out on only root core and broadcasted to the other process cores. In comparison, Lanczos-CG calculates the state vector increment based on the cost function gradient alone (without the need for $J(\mathbf{x})$). The calculation is carried out on each processor core. The above difference has implications for memory requirements: The main memory allocation for L-BFGS-B is its workspace array, which is about $(2 \times k + 4) \times n$, where n is the size of the state vector (x), and k is the number of corrections used in the limited memory matrix. This memory allocation is only needed on the root core. The value of k is set by the user and the recommended value is between 3 and 20. In comparison, Lanczos-CG requires memory size of about $m \times n$ on each processor core, where m is the maximal inner loop iteration allowed. Although it is possible to reduce the per processor core a memory allocation from $m \times n$ to n by disactivating the

modified Gram-Schmidt orthonormalization step, it is typically not recommened.

Another consideration for memory requirements is related to I/O time cost. WRFPLUS saves its entire trajectory in memory to avoid expensive I/O operations. This is not a practical solution for WRF-CO2 4DVar, which is designed to run a longer simulation than the typical 6-hour run intended for WRFDA. GH15/17 implemented a second-order checkpoint mechanism to overcome the memory limit. This approach breaks the whole simulation period into sections, saves restart files at end of each section by the forward model. This approach requires extra calls of the forward model to recalculate the trajectory for each section during backward integration (See Fig. 3 of GH15)

To overcome the memory limit posed by a long simulation, a different approach was implemented. In WRF-CO2 4DVar, the forward model saves the trajectory at each time step in memory, as WRFPLUS does. After a number of integration steps, the memory on each task processor core is dumped to an external file, and the memory is then reused. Each external file is marked with its starting timestamp and the processor core it belongs to. For instance, a 24-hour simulation with 120-second time step will have a total of 720 steps. If the system saves its trajectory to external files each 30 time steps, memory allocation on each task processor core is only needed for 30 steps instead of 720 steps. This will results in 24 $(720/30)$ trajectory files on each task processor core, and the total number of trajectory files depends on the number of processor core used. These trajectory files are read by both tangent linear and adjoint models in a similar way as standard WRF auxiliary files. In the above example, they are read in at each 30 time steps, substantially reducing I/O time compared with reading in at each step. These trajectory files are different from standard WRF auxillary files in that each file belongs to an individual processor core, rather than being shared among all processor cores. This means all model runs in an inverse experiment must use the same domain patch configuration, which is the most common practice.

In future development, we plan to implement observation operators for real observations, including those from towers, satellites, and airborne. This is required for applying WRF-CO2 4DVar with real observation data. As a regional inverse system, correct treatment of chemistry lateral boundary conditions is important. We plan to include chemistry initial and boundary conditions in the state vector in the next update. In addition, future applications of WRF-CO2 4DVar with real observations must use proper treatment of observation and background error covariance, which was not tackled in the pseudo-observation test used in the present paper.

In addition, we also plan to periodically update the WRF-CO2 4DVar system to keep up with WRF system updates. Such updates will mainly consist of replacing the forward model with the updated WRF code, and developing the tangent linear and adjoint code for the relevant updated procedures. As the variable dependence analysis (Section 2.4.2) indicates that the tangent linear and adjoint code are only needed for a portion of WRF procedures, the amount of work required for updating WRF-CO2 4DVar is manageable. In addition, future development of WRF-CO2 4DVar will also be dependent on updates to WRFPLUS, which has always been updated along with WRF.

5 Code availability

WRF-CO2 4DVar source code can be retrieved via https://doi.org/10.5281/zenodo.839260

Acknowledgements. The authors express their appreciation for the WRF/WRF-Chem/WRFDA/WRFPLUS development teams for making their code available in the public domain. Discussion with Joel LeBlanc of Michigan Technological Research Institute (MTRI) improved the optimization schemes implementation and presentation in this paper. The insightful and detailed comments from the two referees greatly improved both the model and the paper. This work was partially supported by a Central Michigan University CST research incentive fund.

References

Alden, C. B., Miller, J. B., Gatti, L. V., Gloor, M. M., Guan, K., Michalak, A. M., van der Laan-Luijkx, I. T., Touma, D., Andrews, A., Basso, L. S., Correia, C. S. C., Domingues, L. G., Joiner, J., Krol, M. C., Lyapustin, A. I., Peters, W., Shiga, Y. P., Thoning, K., van der Velde, I. R., van Leeuwen, T. T., Yadav, V., and Diffenbaugh, N. S.: Regional atmospheric CO2 inversion reveals seasonal and geographic differences in Amazon net biome exchange, Global Change Biol., 22, 3427–3443, doi:10.1111/gcb.13305, 2016.

Baker, D. F., Doney, S. C., and Schimel, D. S.: Variational data assimilation for atmospheric CO2, Tellus Ser. B-Chemical and Physical Meteorology, 58, 359–365, 2006.

Baker, D. F., Boesch, H., Doney, S. C., O'Brien, D., and Schimel, D. S.: Carbon source/sink information provided by column CO2 measurements from the Orbiting Carbon Observatory, Atmos. Chem. Phys., 10, 4145–4165, 2010.

Barker, D., Huang, X.-Y., Liu, Z., Auligne, T., Zhang, X., Rugg, S., Ajjaji, R., Bourgeois, A., Bray, J., Chen, Y., Demirtas, M., Guo, Y.-R., Henderson, T., Huang, W., Lin, H.-C., Michalakes, J., Rizvi, S., and Zhang, X.: The Weather Research and Forecasting Model's Community Variational/Ensemble Data Assimilation System WRFDA, Bull. Amer. Meteor. Soc., 93, 831–843, 2012.

Basu, S., Houweling, S., Peters, W., Sweeney, C., Machida, T., Maksyutov, S., Patra, P. K., Saito, R., Chevallier, F., Niwa, Y., Matsueda, H., and Sawa, Y.: The seasonal cycle amplitude of total column CO2: Factors behind the model-observation mismatch, J. Geophys. Res.-Atmospheres, 116, d23306, 2011.

Basu, S., Guerlet, S., Butz, A., Houweling, S., Hasekamp, O., Aben, I., Krummel, P., Steele, P., Langenfelds, R., Torn, M., Biraud, S., Stephens, B., Andrews, A., and Worthy, D.: Global CO2 fluxes estimated from GOSAT retrievals of total column CO2, Atmos. Chem. Phys., 13, 8695–8717, doi:10.5194/acp-13-8695-2013, 2013.

Bocquet, M.: Toward Optimal Choices of Control Space Representation for Geophysical Data Assimilation, Mon. Weather Rev., 137, 2331–2348, 2009.

Butler, M. P., Davis, K. J., Denning, A. S., and Kawa, S. R.: Using continental observations in global atmospheric inversions of CO2: North American carbon sources and sinks, Tellus Ser. B-Chemical and Physical Meteorology, 62, 550–572, 2010.

Byrd, R. H., Lu, P., and Nocedal, J.: A limited memory algorithm for bound constrained optimization, SIAM Journal on Scientific and Statistical Computing, 16, 1190–1208, 1995.

Chan, E., Chan, D., Ishizawa, M., Vogel, F., Brioude, J., Delcloo, A., Wu, Y., and Jin, B.: Description and evaluation of REFIST v1.0: a regional greenhouse gas flux inversion system in Canada, Geosci. Model Dev. Discussion, doi:https://doi.org/10.519/gmd-2016-213, 2016.

Chevallier, F.: Impact of correlated observation errors on inverted CO2 surface fluxes from OCO measurements, Geophys. Res. Lett., 34, doi:10.1029/2007GL030463, 2007.

Chevallier, F., Fisher, M., Peylin, P., Serrar, S., Bousquet, P., Breon, F. M., Chedin, A., and Ciais, P.: Inferring CO2 sources and sinks from satellite observations: Method and application to TOVS data, J. Geophys. Res.-Atmospheres, 110, d24309, 2005.

Chevallier, F., Ciais, P., Conway, T. J., Aalto, T., Anderson, B. E., Bousquet, P., Brunke, E. G., Ciattaglia, L., Esaki, Y., Froehlich, M., Gomez, A., Gomez-Pelaez, A. J., Haszpra, L., Krummel, P. B., Langenfelds, R. L., Leuenberger, M., Machida, T., Maignan, F., Matsueda, H., Morgui, J. A., Mukai, H., Nakazawa, T., Peylin, P., Ramonet, M., Rivier, L., Sawa, Y., Schmidt, M., Steele, L. P., Vay, S. A., Vermeulen, A. T., Wofsy, S., and Worthy, D.: CO2 surface fluxes at grid point scale estimated from a global 21 year reanalysis of atmospheric measurements, J. Geophys. Res.-Atmospheres, 115, d21307, 2010.

Chou, M. D. and Suarez, M.: A solar radiation parameterization for atmospheric studies, Tech. Rep. NASA/TM-1999-10460, vol. 15, 38 pp, NASA, 1999.

Ciais, P., Dolman, A. J., Bombelli, A., Duren, R., Peregon, A., Rayner, P. J., Miller, C., Gobron, N., Kinderman, G., Marland, G., Gruber, N., Chevallier, F., Andres, R. J., Balsamo, G., Bopp, L., Breon, F. M., Broquet, G., Dargaville, R., Battin, T. J., Borges, A., Bovensmann, H., Buchwitz, M., Butler, J., Canadell, J. G., Cook, R. B., DeFries, R., Engelen, R., Gurney, K. R., Heinze, C., Heimann, M., Held, A., Henry, M., Law, B., Luyssaert, S., Miller, J., Moriyama, T., Moulin, C., Myneni, R. B., Nussli, C., Obersteiner, M., Ojima, D., Pan, Y., Paris, J. D., Piao, S. L., Poulter, B., Plummer, S., Quegan, S., Raymond, P., Reichstein, M., Rivier, L., Sabine, C., Schimel, D., Tarasova, O., Valentini, R., Wang, R., van der Werf, G., Wickland, D., Williams, M., and Zehner, C.: Current systematic carbon-cycle observations and the need for implementing a policy-relevant carbon observing system, Biogeosciences, 11, 3547–3602, doi:10.5194/bg-11-3547-2014, 2014.

Deng, F., Jones, D. B. A., Henze, D. K., Bousserez, N., Bowman, K. W., Fisher, J. B., Nassar, R., O'Dell, C., Wunch, D., Wennberg, P. O., Kort, E. A., Wofsy, S. C., Blumenstock, T., Deutscher, N. M., Griffith, D. W. T., Hase, F., Heikkinen, P., Sherlock, V., Strong, K., Sussmann, R., and Warneke, T.: Inferring regional sources and sinks of atmospheric CO2 from GOSAT XCO2 data, Atmos. Chem. Phys., 14, 3703–3727, 2014.

Fowler, A. M. and Lawless, A. S.: An Idealized Study of Coupled Atmosphere–Ocean 4D-Var in the presence of model error, Mon. Weather Rev., 144, 4007–4029, doi:10.1175/MWR-D-15-0420.1, 2016.

Freitas, S. R., Longo, K. M., Alonso, M. F., Pirre, M., Marecal, V., Grell, G., Stockler, R., Mello, R. F., and Sanchez Gacita, M.: PREP-CHEM-SRC-1.0: a preprocessor of trace gas and aerosol emission fields for regional and global atmospheric chemistry models, Geosci. Model Dev., 4, 419–433, 2010.

French, N. H. F., de Groot, W. J., Jenkins, L. K., Rogers, B. M., Alvarado, E., Amiro, B., de Jong, B., Goetz, S., Hoy, E., Hyer, E., Keane, R., Law, B. E., McKenzie, D., McNulty, S. G., Ottmar, R., Perez-Salicrup, D. R., Randerson, J., Robertson, K. M., and Turetsky, M.: Model comparisons for estimating carbon emissions from North American wildland fire, J. Geophys. Res., 116, doi:10.1029/2010JG001469, 2011.

Gerbig, C., Lin, J. C., Wofsy, S. C., Daube, B. C., Andrews, A. E., Stephens, B. B., Bakwin, P. S., and Grainger, C. A.: Toward constraining regional-scale fluxes of CO2 with atmospheric observations over a continent: 1. Observed spatial variability from airborne platforms, J. Geophys. Res.-Atmospheres, 108, 4756, 2003.

Gerbig, C., Korner, S., and Lin, J. C.: Vertical mixing in atmospheric tracer transport models: error characterization and propagation, Atmos. Chem. Phys., 8, 591–602, 2008.

Gerbig, C., Dolman, A. J., and Heimann, M.: On observational and modelling strategies targeted at regional carbon exchange over continents, Biogeosciences, 6, 1949–1959, 2009.

Grell, G. A. and Freitas, S. R.: A scale and aerosol aware stochastic convective parameterization for weather and air quality modeling, Atmos. Chem. Phys., 14, 5233–5250, doi:10.5194/acp-14-5233-2014, 2014.

Grell, G. A., Knoche, R., Peckham, S. E., and McKeen, S. A.: Online versus offline air quality modeling on cloud-resolving scales, Geophys. Res. Lett., 31, l16117, 2004.

Grell, G. A., Peckham, S. E., Schmitz, R., McKeen, S. A., Frost, G., Skamarock, W. C., and Eder, B.: Fully coupled online chemistry within the WRF model, Atmos. Environ., 39, 6957–6975, 2005.

Guerrette, J. J. and Henze, D. K.: Development and application of the WRFPLUS-Chem online chemistry adjoint and WRFDA-Chem assimilation system, Geosci. Model Dev., 8, 1857–1876, 2015.

Guerrette, J. J. and Henze, D. K.: Four dimensional variation of black carbon emissions during ARACTAS-CARB with WRFDA-Chem, Atmos. Chem. Phys., doi:10.5194/acp-17-7605-2017, 2017.

Gurney, K. R., Chen, Y. H., Maki, T., Kawa, S. R., Andrews, A., and Zhu, Z. X.: Sensitivity of atmospheric CO2 inversions to seasonal and interannual variations in fossil fuel emissions, J. Geophys. Res.-Atmospheres, 110, d10308, 2005.

Hascoet, L. and Pascual, V.: The Tapenade Automatic Differentiation Tool: Principles, Model, and Specification, ACM Trans. Math. Software, 39, 20, 2013.

Henze, D. K., Hakami, A., and Seinfeld, J. H.: Development of the adjoint of GEOS-Chem, Atmos. Chem. Phys., 7, 2413–2433, 2007.

Hourdin, F., Musat, I., Bony, S., Braconnot, P., Codron, F., Dufresne, J. L., Fairhead, L., Filiberti, M. A., Friedlingstein, P., Grandpeix, J. Y., Krinner, G., Levan, P., Li, Z. X., and Lott, F.: The LMDZ4 general circulation model: climate performance and sensitivity to parametrized physics with emphasis on tropical convection, Climate Dyn., 27, 787–813, 2006.

Houweling, S., Aben, I., Breon, F. M., Chevallier, F., Deutscher, N., Engelen, R., Gerbig, C., Griffith, D., Hungershoefer, K., Macatangay, R., Marshall, J., Notholt, J., Peters, W., and Serrar, S.: The importance of transport model uncertainties for the estimation of CO2 sources and sinks using satellite measurements, Atmos. Chem. Phys., 10, 9981–9992, 2010.

Huang, X.-Y., Xiao, Q., Barker, D. M., Zhang, X., Michalakes, J., Huang, W., Henderson, T., Bray, J., Chen, Y., Ma, Z., Dudhia, J., Guo, Y., Zhang, X., Won, D.-J., Lin, H.-C., and Kuo, Y.-H.: Four-Dimensional Variational Data Assimilation for WRF: Formulation and Preliminary Results, Mon. Weather Rev., 137, 299–314, 2009.

Jiang, X., Li, Q. B., Liang, M. C., Shia, R. L., Chahine, M. T., Olsen, E. T., Chen, L. L., and Yung, Y. L.: Simulation of upper tropospheric CO2 from chemistry and transport models, Global Biogeochem. Cycles, 22, gB4025, 2008.

Kaminski, T., Rayner, P. J., Heimann, M., and Enting, I. G.: On aggregation errors in atmospheric transport inversions, J. Geophys. Res.-Atmospheres, 106, 4703–4715, 2001.

Kawa, S. R., Erickson, D. J., Pawson, S., and Zhu, Z.: Global CO2 transport simulations using meteorological data from the NASA data assimilation system, J. Geophys. Res.-Atmospheres, 109, d18312, 2004.

Kopacz, M., Jacob, D. J., Henze, D. K., Heald, C. L., Streets, D. G., and Zhang, Q.: Comparison of adjoint and analytical Bayesian inversion methods for constraining Asian sources of carbon monoxide using satellite (MOPITT) measurements of CO columns, J. Geophys. Res.-Atmospheres, 114, d04305, 2009.

Krol, M., Houweling, S., Bregman, B., van den Broek, M., Segers, A., van Velthoven, P., Peters, W., Dentener, F., and Bergamaschi, P.: The two-way nested global chemistry-transport zoom model TM5: algorithm and applications, Atmos. Chem. Phys., 5, 417–432, 2005.

Lanczos, C.: An Iteration Method for the Solution of the Eigenvalue Problem of Linear Differential and Integral Operators, J. Res. Nat. Bur. Stand., 45, 255–282, 1950.

Lauvaux, T., Schuh, A. E., Uliasz, M., Richardson, S., Miles, N., Andrews, A. E., Sweeney, C., Diaz, L. I., Martins, D., Shepson, P. B., and Davis, K. J.: Constraining the CO2 budget of the corn belt: exploring uncertainties from the assumptions in a mesoscale inverse system, Atmos. Chem. Phys., 12, 337–354, 2012.

Lin, J. C., Gerbig, C., Wofsy, S. C., Andrews, A. E., Daube, B. C., Davis, K. J., and Grainger, C. A.: A near-field tool for simulating the upstream influence of atmospheric observations: The Stochastic Time-Inverted Lagrangian Transport (STILT) model, J. Geophys. Res.-Atmospheres, 108, 4493, 2003.

Liu, J., Bowman, K. W., Lee, M., Henze, D. K., Bousserez, N., Brix, H., Collatz, G. J., Menemenlis, D., Ott, L., Pawson, S., Jones, D., and Nassar, R.: Carbon monitoring system flux estimation and attribution: impact of ACOS-GOSAT X-CO2 sampling on the inference of terrestrial biospheric sources and sinks, Tellus Ser. B, 66, doi:10.3402/tellusb.v66.22486, 2014.

Luis Morales, J. and Nocedal, J.: Remark on "Algorithm 778: L-BFGS-B: Fortran Subroutines for Large-Scale Bound Constrained Optimization", ACM Trans. Math. Software, 38, doi:10.1145/2049662.2049669, 2011.

Mahadevan, P., Wofsy, S. C., Matross, D. M., Xiao, X. M., Dunn, A. L., Lin, J. C., Gerbig, C., Munger, J. W., Chow, V. Y., and Gottlieb, E. W.: A satellite-based biosphere parameterization for net ecosystem CO2 exchange: Vegetation Photosynthesis and Respiration Model (VPRM), Global Biogeochem. Cycles, 22, gB2005, 2008.

Meirink, J. F., Bergamaschi, P., Frankenberg, C., d'Amelio, M. T. S., Dlugokencky, E. J., Gatti, L. V., Houweling, S., Miller, J. B., Roeckmann, T., Villani, M. G., and Krol, M. C.: Four-dimensional variational data assimilation for inverse modeling of atmospheric methane emissions: Analysis of SCIAMACHY observations, J. Geophys. Res.-Atmospheres, 113, d17301, 2008.

Mlawer, E., Taubman, S., Brown, P., Iacono, M., and Clough, S.: Radiative transfer for inhomogeneous atmospheres: RRTM, a validated correlated-k model for the longwave, J. Geophys. Res., 102, 16 663–16 682, doi:10.1029/97JD00237, 1997.

Nassar, R., Jones, D. B. A., Suntharalingam, P., Chen, J. M., Andres, R. J., Wecht, K. J., Yantosca, R. M., Kulawik, S. S., Bowman, K. W., Worden, J. R., Machida, T., and Matsueda, H.: Modeling global atmospheric CO2 with improved emission inventories and CO2 production from the oxidation of other carbon species, Geosci. Model Dev., 3, 689–716, 2010.

Nassar, R., Jones, D. B. A., Kulawik, S. S., Worden, J. R., Bowman, K. W., Andres, R. J., Suntharalingam, P., Chen, J. M., Brenninkmeijer, C. A. M., Schuck, T. J., Conway, T. J., and Worthy, D. E.: Inverse modeling of CO2 sources and sinks using satellite observations of CO2 from TES and surface flask measurements, Atmos. Chem. Phys., 11, 6029–6047, 2011.

Nehrkorn, T., Eluszkiewicz, J., Wofsy, S. C., Lin, J. C., Gerbig, C., Longo, M., and Freitas, S.: Coupled weather research and forecasting-stochastic time-inverted lagrangian transport (WRF-STILT) model, Meteorol. Atmos. Phys., 107, 51–64, 2010.

Ott, L., Pawson, S., Collatz, G., Gregg, W. W., Menemenlis, D., Brix, H., Rosseaux, C. S., Bowman, K. W., Liu, J., Eldering, A., Gunson, M. R., and Kawa, S. R.: Assessing the magnitude of CO2 flux uncertainty in atmospheric CO2 records using products from NASA's Carbon Monitoring Flux Pilot Project, J. Geophys. Res.: Atmosphere, 120, doi:10.1002/2014JD022 411, 2015.

Peters, W., Jacobson, A. R., Sweeney, C., Andrews, A. E., Conway, T. J., Masarie, K., Miller, J. B., Bruhwiler, L. M. P., Petron, G., Hirsch, A. I., Worthy, D. E. J., van der Werf, G. R., Randerson, J. T., Wennberg, P. O., Krol, M. C., and Tans, P. P.: An atmospheric perspective on North American carbon dioxide exchange: CarbonTracker, Proc. Natl. Acad. Sci. U.S.A., 104, 18 925–18 930, 2007.

Pillai, D., Gerbig, C., Kretschmer, R., Beck, V., Karstens, U., Neininger, B., and Heimann, M.: Comparing Lagrangian and Eulerian models for CO2 transport - a step towards Bayesian inverse modeling using WRF/STILT-VPRM, Atmos. Chem. Phys., 12, 8979–8991, 2012.

Pleim, J. E.: A simple, efficient solution of flux-profile relationships in the atmospheric surface layer, J. Appl. Meteorol. and Climatology, 45, 341–347, 2006.

Pleim, J. E.: A combined local and nonlocal closure model for the atmospheric boundary layer. Part I: Model description and testing, J. Appl. Meteorol. and Climatology, 46, 1383–1395, 2007.

Pleim, J. E. and Xiu, A. J.: Development of a land surface model. Part II: Data assimilation, J. Appl. Meteorol., 42, 1811–1822, 2003.

Rabier, F., Jarvinen, H., Klinker, E., Mahfouf, J. F., and Simmons, A.: The ECMWF operational implementation of four-dimensional variational assimilation. I: Experimental results with simplified physics, Quart. J. Roy. Meteor. Soc., 126, 1143–1170, a, 2000.

Saha, S., Moorthi, S., Wu, X., Wang, J., Nadiga, S., Tripp, P., Behringer, D., Hou, Y.-T., Chuang, H.-Y., Iredell, M., Ek, M., Meng, J., Yang, R., Mendez, M. P., Van Den Dool, H., Zhang, Q., Wang, W., Chen, M., and Becker, E.: The NCEP Climate Forecast System Version 2, J. Climate, 27, 2185–2208, doi:10.1175/JCLI-D-12-00823.1, 2014.

Saito, R., Houweling, S., Patra, P. K., Belikov, D., Lokupitiya, R., Niwa, Y., Chevallier, F., Saeki, T., and Maksyutov, S.: TransCom satellite intercomparison experiment: Construction of a bias corrected atmospheric CO2 climatology, J. Geophys. Res.-Atmospheres, 116, d21120, 2011.

Smith, A., Lott, N., and Vose, R.: The Integrated Surface Database Recent Developments and Partnerships, Bull. Amer. Meteor. Soc., 92, 704–708, doi:10.1175/2011BAMS3015.1, 2011.

Stein, A. F., Draxler, R. R., Rolph, G. D., Stunder, B. J. B., Cohen, M. D., and Ngan, F.: NOAA'S HYSPLIT atmospheric transport and dispersion modeling system, Bull. Amer. Meteor. Soc., 96, 2059–2077, doi:10.1175/BAMS-D-14-00110.1, 2015.

Stephens, B. B., Gurney, K. R., Tans, P. P., Sweeney, C., Peters, W., Bruhwiler, L., Ciais, P., Ramonet, M., Bousquet, P., Nakazawa, T., Aoki, S., Machida, T., Inoue, G., Vinnichenko, N., Lloyd, J., Jordan, A., Heimann, M., Shibistova, O., Langenfelds, R. L., Steele, L. P., Francey, R. J., and Denning, A. S.: Weak northern and strong tropical land carbon uptake from vertical profiles of atmospheric CO(2), Science, 316, 1732–1735, 2007.

Stohl, A., Forster, C., Frank, A., Seibert, P., and Wotawa, G.: Technical note: The Lagrangian particle dispersion model FLEXPART version 6.2, Atmos. Chem. Phys., 5, 2461–2474, 2005.

Thompson, G., Field, P. R., Rasmussen, R. M., and Hall, W. D.: Explicit forecasts of winter precipitation using an improved bulk microphysics scheme. Part II: implementation of a new snow parameterization, Mon. Weather Rev., 136, 5095–5115, 2008.

Tremolet, Y.: Diagnostics of linear and incremental approximations in 4D-Var, Quart. J. Roy. Meteor. Soc., 130, 2233–2251, b, 2004.

Turner, A. J. and Jacob, D. J.: Balancing aggregation and smoothing errors in inverse models, Atmos. Chem. Phys., 15, 7039–7048, 2015.

Uliasz, M.: The Atmospheric Mesoscale Dispersion Modeling System, J. Appl. Meteorol., 32, 139–149, 1993.

Wecht, K. J., Jacob, D. J., Frankenberg, C., Jiang, Z., and Blake, D. R.: Mapping of North American methane emissions with high spatial resolution by inversion of SCIAMACHY satellite data, J. Geophys. Res.-Atmospheres, 119, 7741–7756, times Cited: 13, 2014.

Yadav, V. and Michalak, A. M.: Improving computational efficiency in large linear Inverse Prob.: an example from carbon dioxide flux estimation, Geosci. Model Dev., 6, 583–590, doi:10.5194/gmd-6-583-2013, 2013.

Zhang, X., Huang, X.-Y., and Pan, N.: Development of the Upgraded Tangent Linear and Adjoint of the Weather Research and Forecasting (WRF) Model, J. Atmos. Oceanic Technol., 30, 1180–1188, 2013.

Zhu, C., Byrd, R., Lu, P., and Nocedal, J.: Algorithm 778: L-BFGS-B: Fortran subroutines for large-scale bound-constrained optimization, ACM Trans. Math. Software, 23, 550–560, doi:10.1145/279232.279236, 1997.

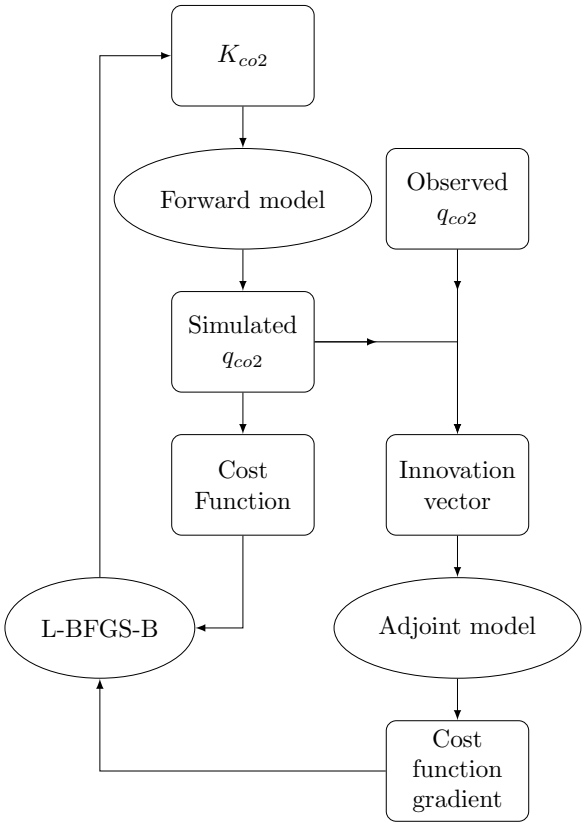

Figure 1. Diagram of L-BFGS-B based optimization implemented for WRF-CO2 4DVar.

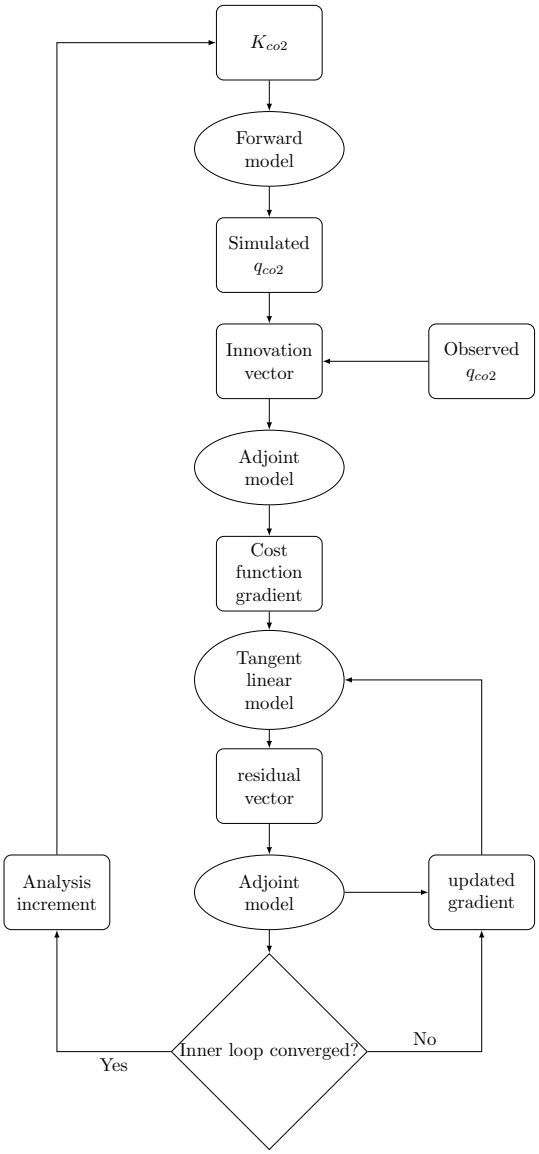

Figure 2. Diagram of Lanczos-CG based incremental optimization implemented for WRF-CO2 4DVar

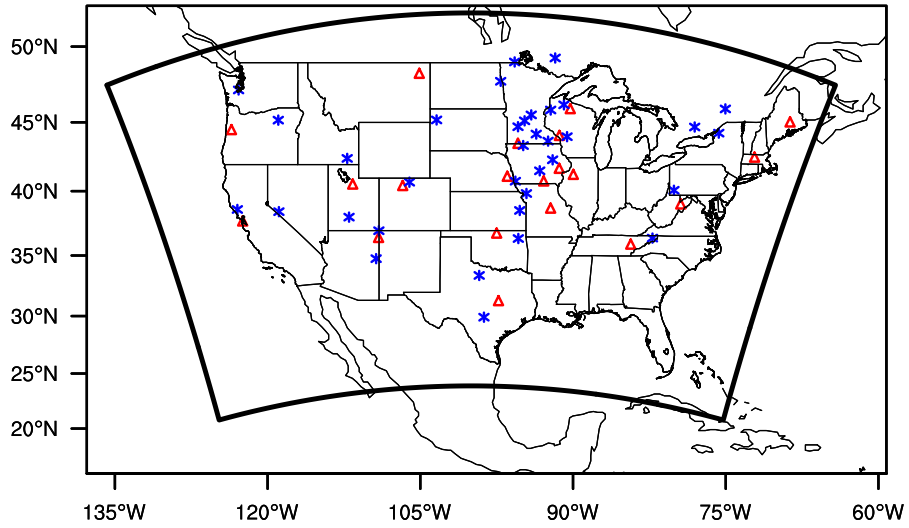

Figure 3. WRF-4DVar simulation domain covering the continental United State with 48 km×48 km grid spacing. The domain boundary is marked by the bold dark outline. Grid cells used for evaluating sensitivities are marked: red triangles are the 20 CO_2 tower sites used as receptor location ; blue starts are source locations. While receptors are placed at the 1^{st}, 5^{th}, and 10^{th} vertical level at each site, all sources are at the 1^{st} level only.

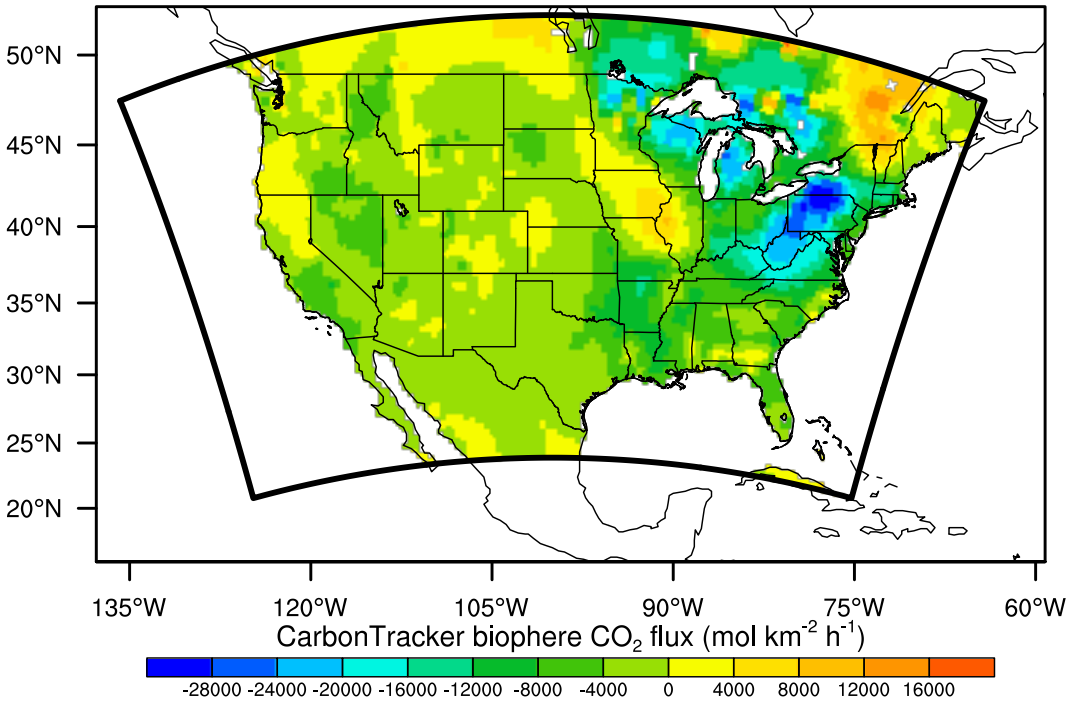

Figure 4. Daily mean CarbonTracker biosphere CO_2 flux, calculated as the arithmetic mean of the 3-hourly flux between 2011-06-02 00:00:00 UTC to 2011-06-03 00:00:00 UTC.

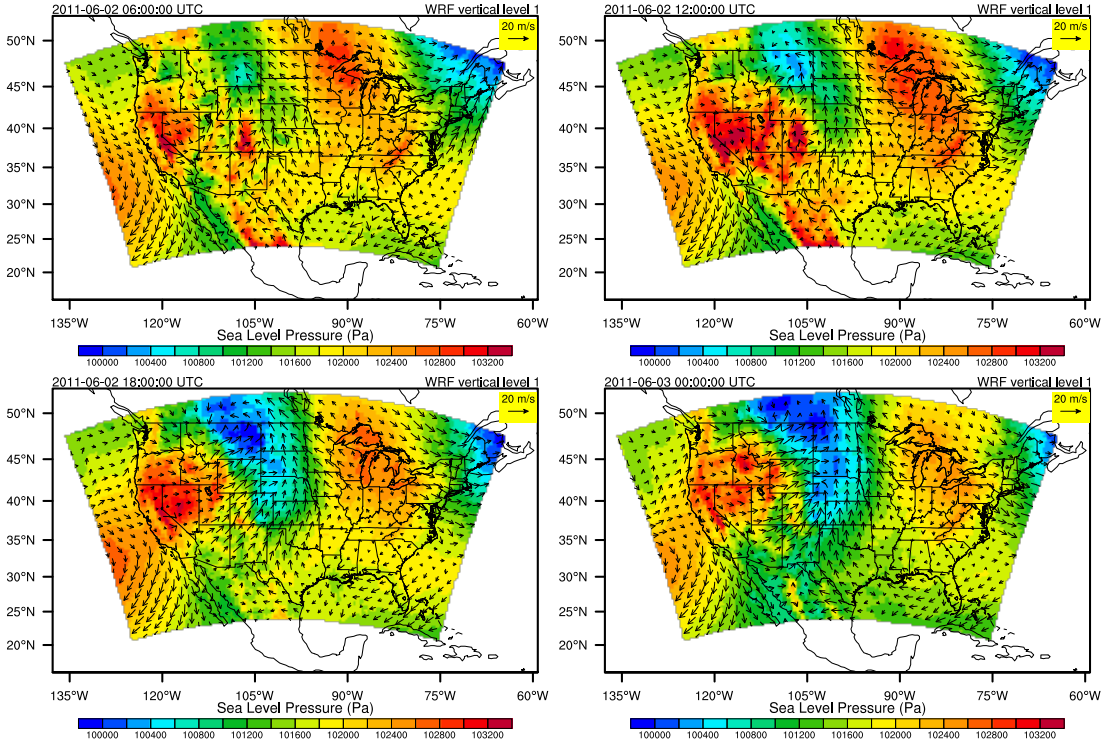

Figure 5. Sea Level Pressure (Pa) and horizontal wind (m s^{-1}) at model's lowest vertical level plotted at 6-hour interval during the 24-hour simulation starting at 2011-06-02 00:00 UTC.

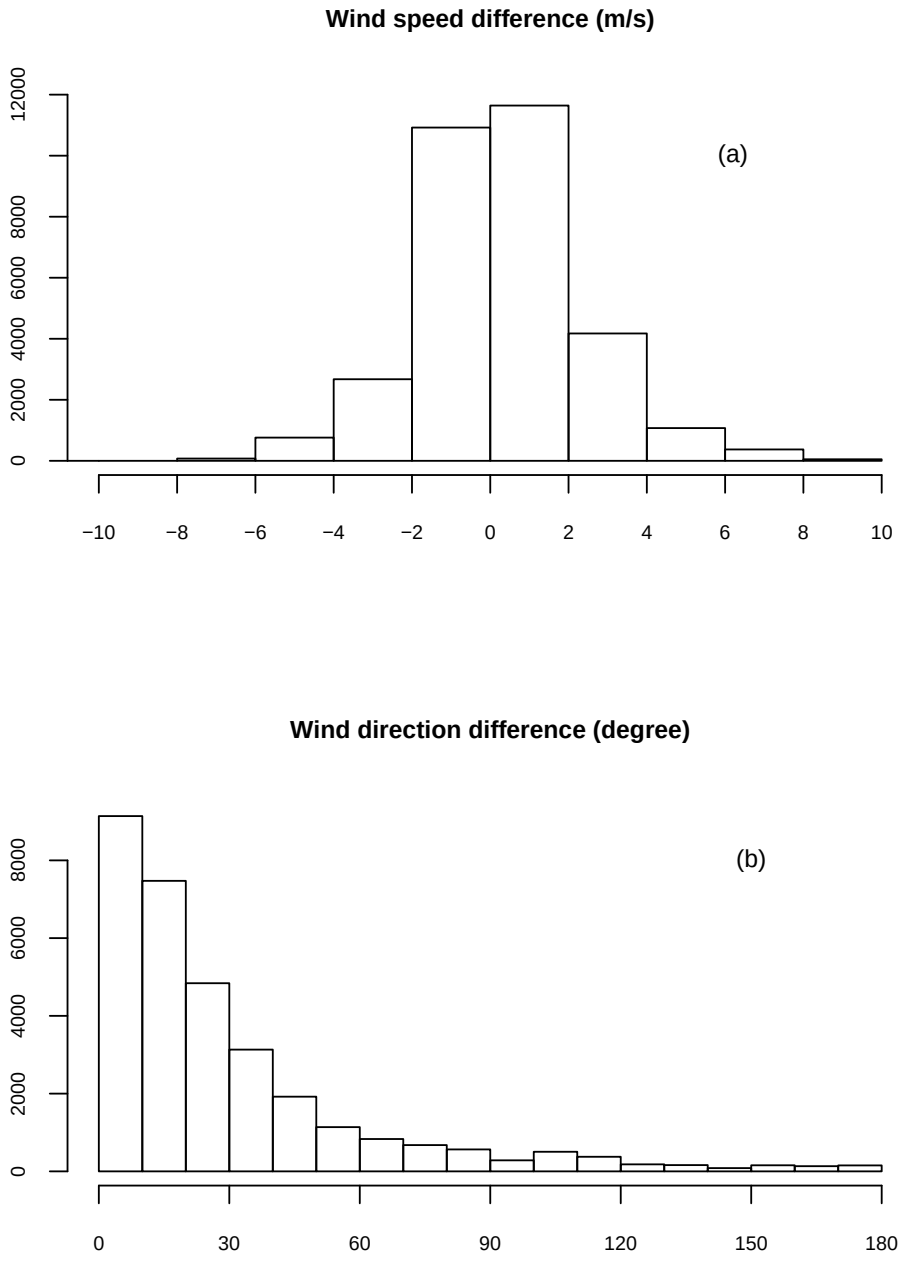

Figure 6. Histograms of the 10m wind speed difference (a) and wind direction difference (b) between WRF simulation and surface meteorological station measurements.

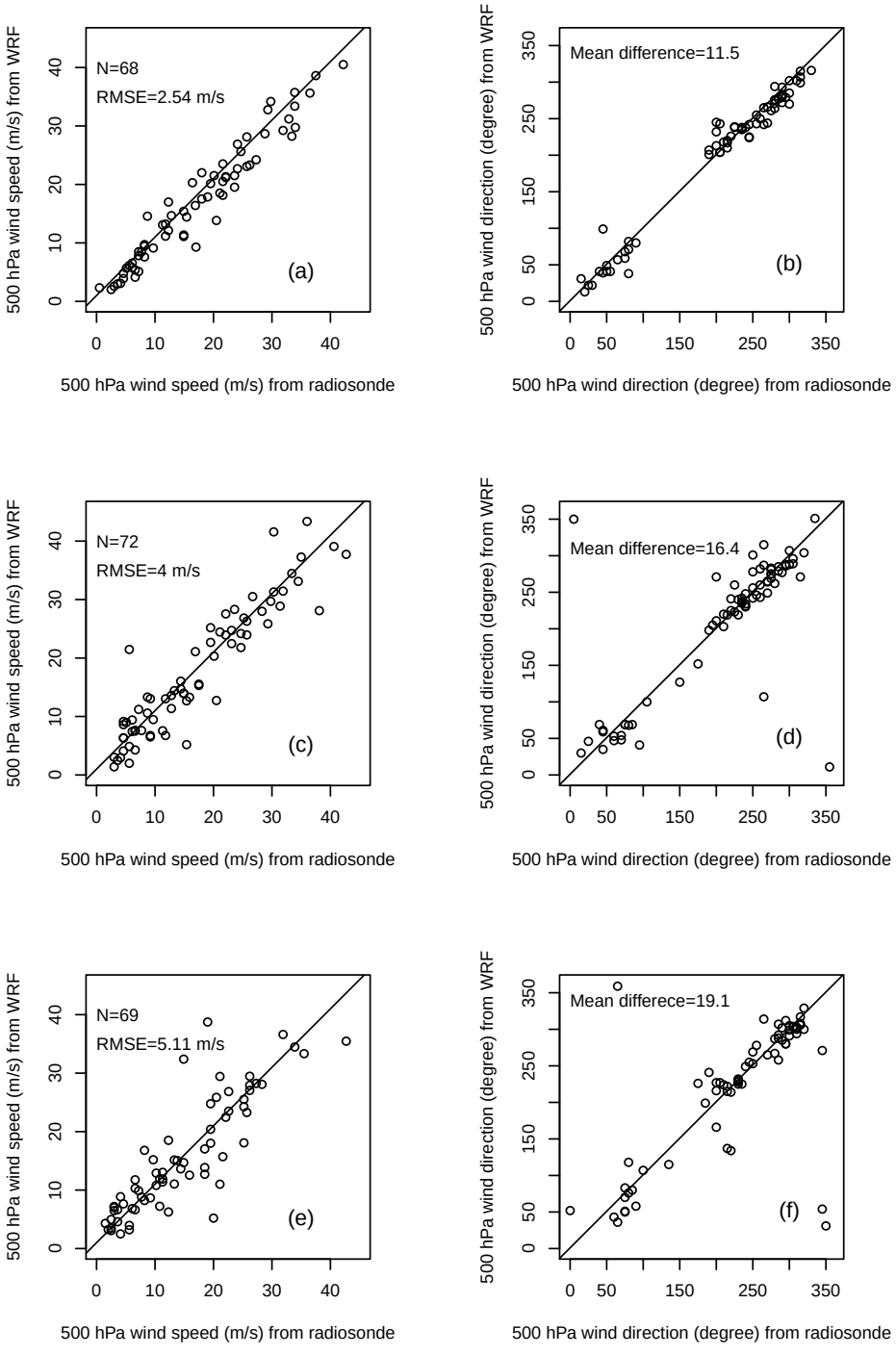

Figure 7. Comparison of 500hPa wind speed and wind direction between WRF simulation and radiosonde measurements. Figures (a) anb (b) are the comparison at 2011-06-02 00:00 UTC; Figures (c) and (d) are at 2011-06-02 12:00 UTC; and Figures (e) and (f) are at 2011-06-03 00:00 UTC. RMSE and relative error (RE) for wind speed and meann difference in wind direction are shown in each figure.

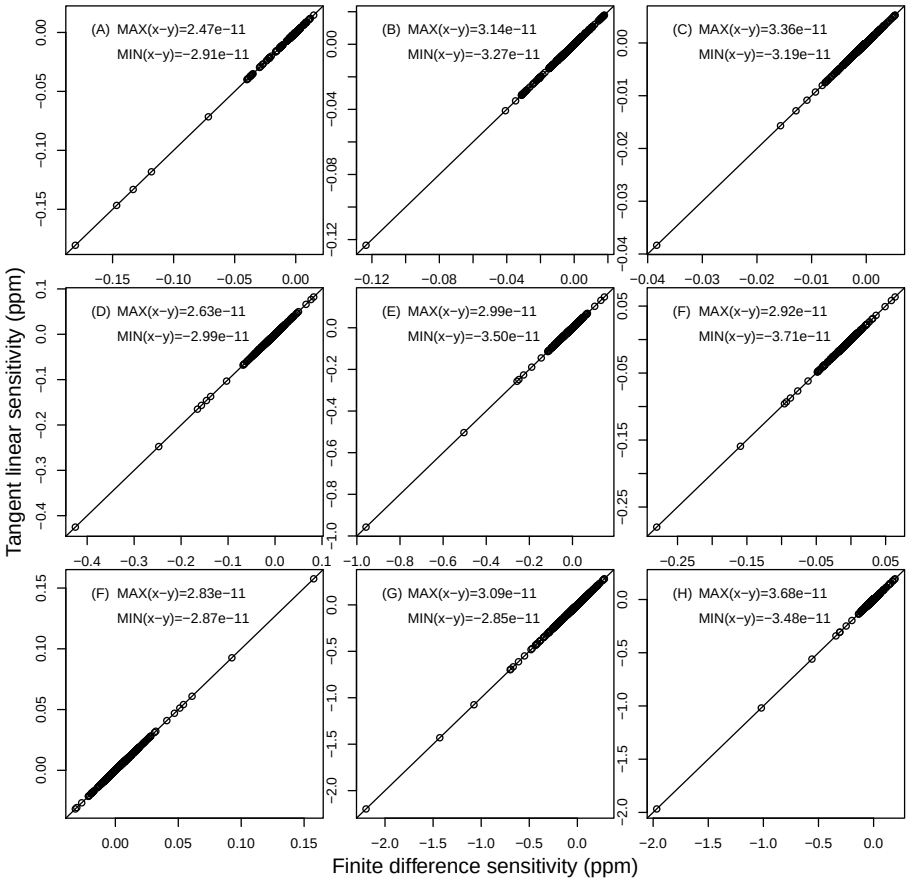

Figure 8. Comparison between $\partial q_{co2}/\partial k_{co2}$ calculated by finite difference (x axis) and tangent linear model (y axis) for nine sources (see Fig. 3 for source locations).

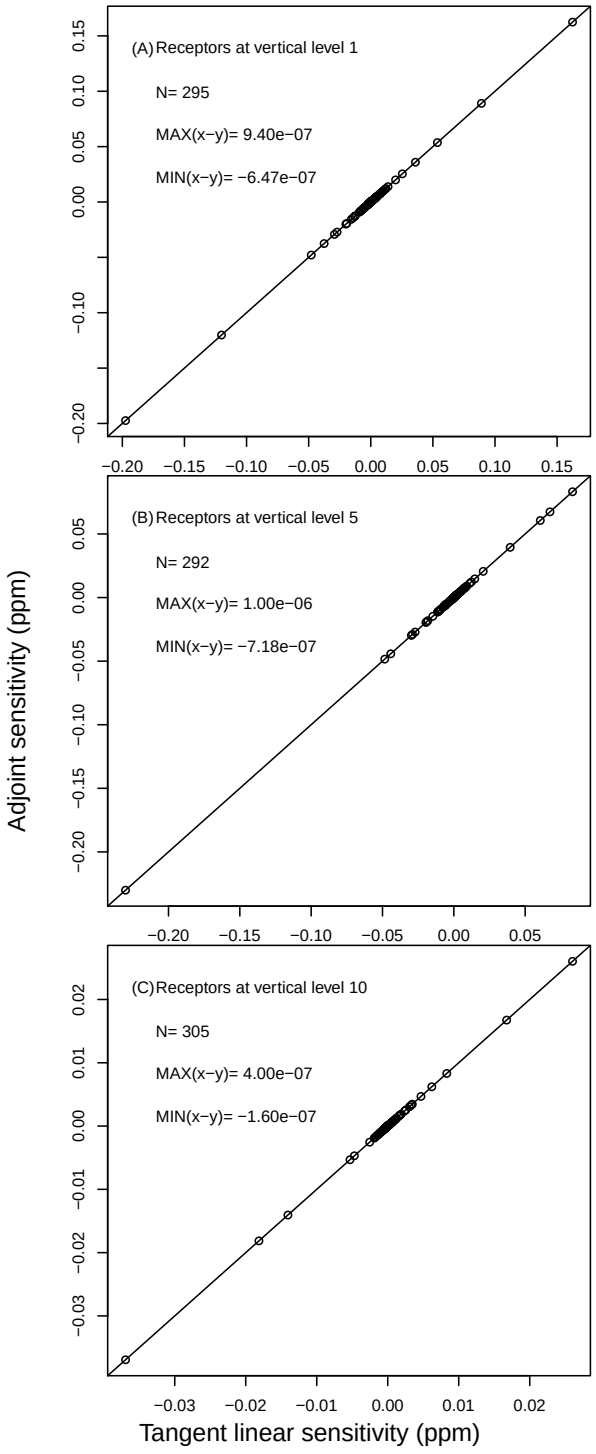

Figure 9. Comparison between $\partial q_{co2}/\partial k_{co2}$ calculated by the tangent linear (x axis) and adjoint model (y axis).

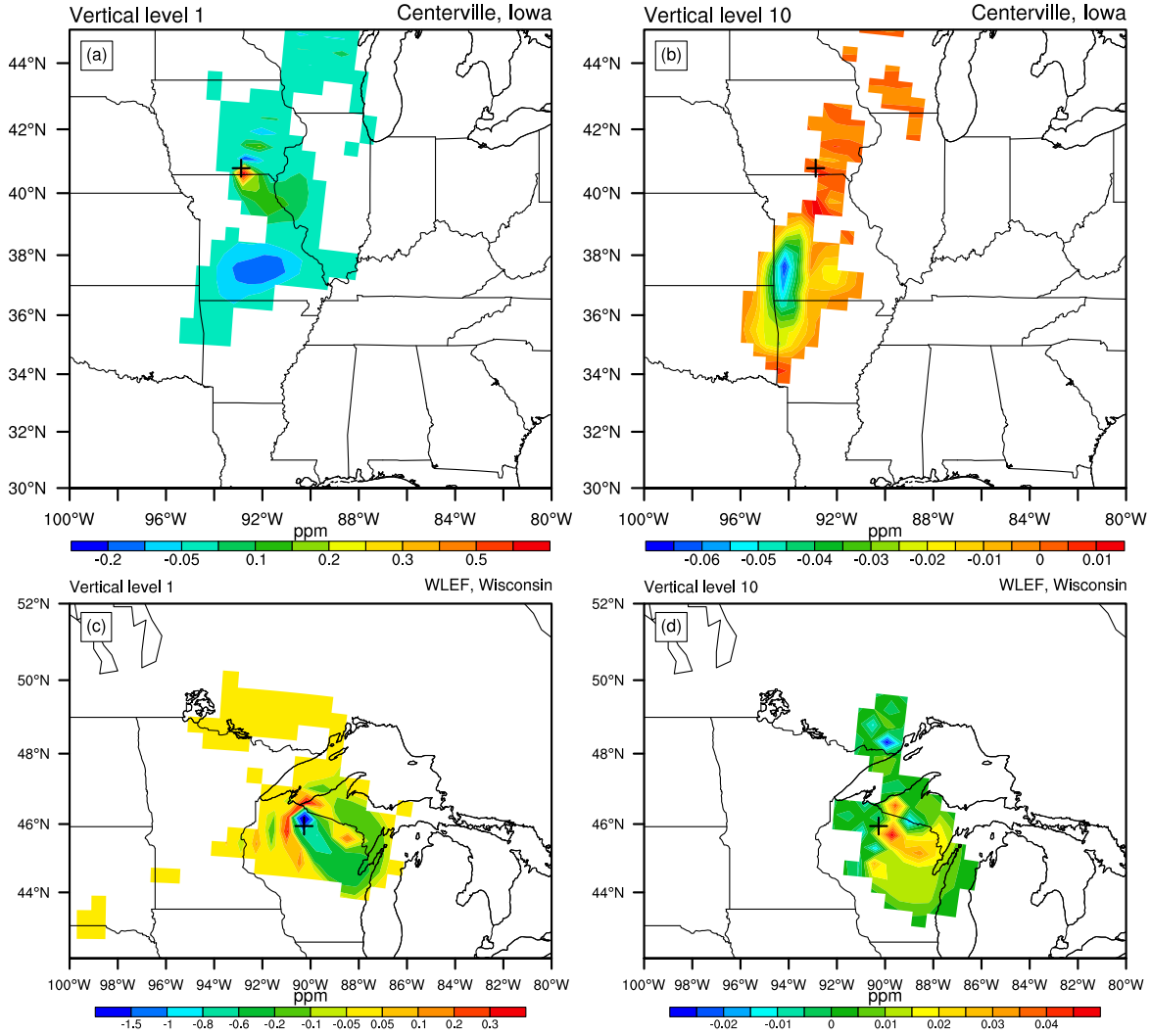

Figure 10. The top panel shows adjoint sensitivity of receptors placed at the 1st (a), and 10th (d) vertical level at Centerville, Iowa. The bottom panel shows adjoint sensitivity of receptors placed at the 1st (c), and 10th (d) vertical level at WLEF, Wisconsin. The black cross in each figure marks the corresponding tower site.

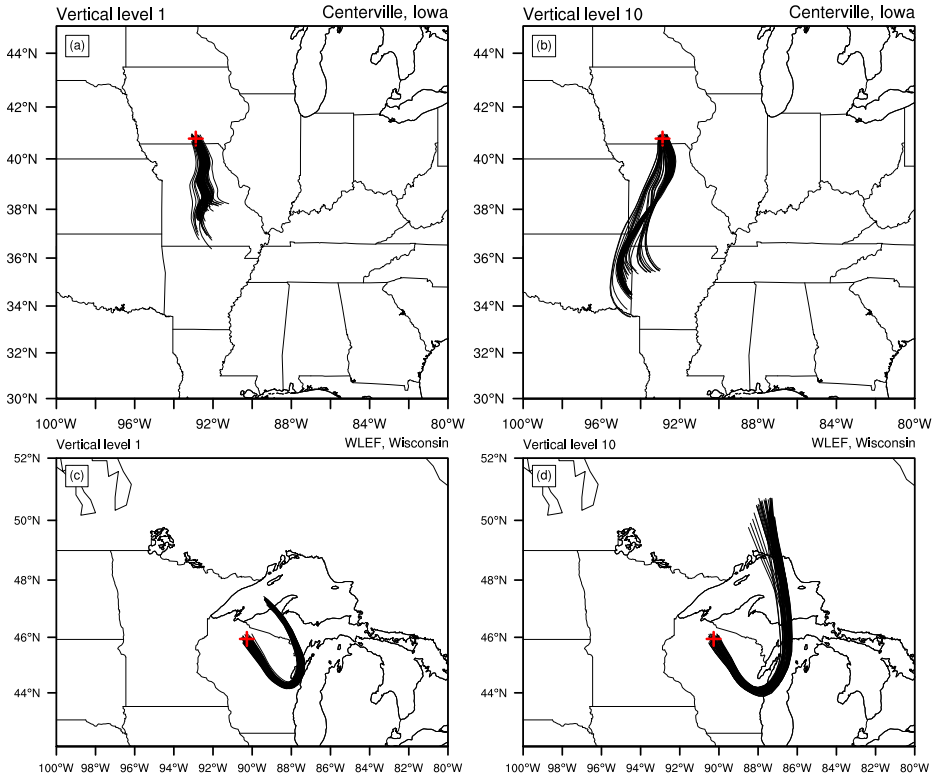

Figure 11. Backward trajectories of particles released from the Centerville, Iowa and WLEF, Wisconsin. The tower sites are marked with red crosses. All particles are released at 2011-06-03 00:00 UTC and transported backward in time for 24 hours. Figures (a) and (c) are the trajectories of particles released from the height match WRF's 1st vertical level, and Figures (b) and (d) are of the 10th level.

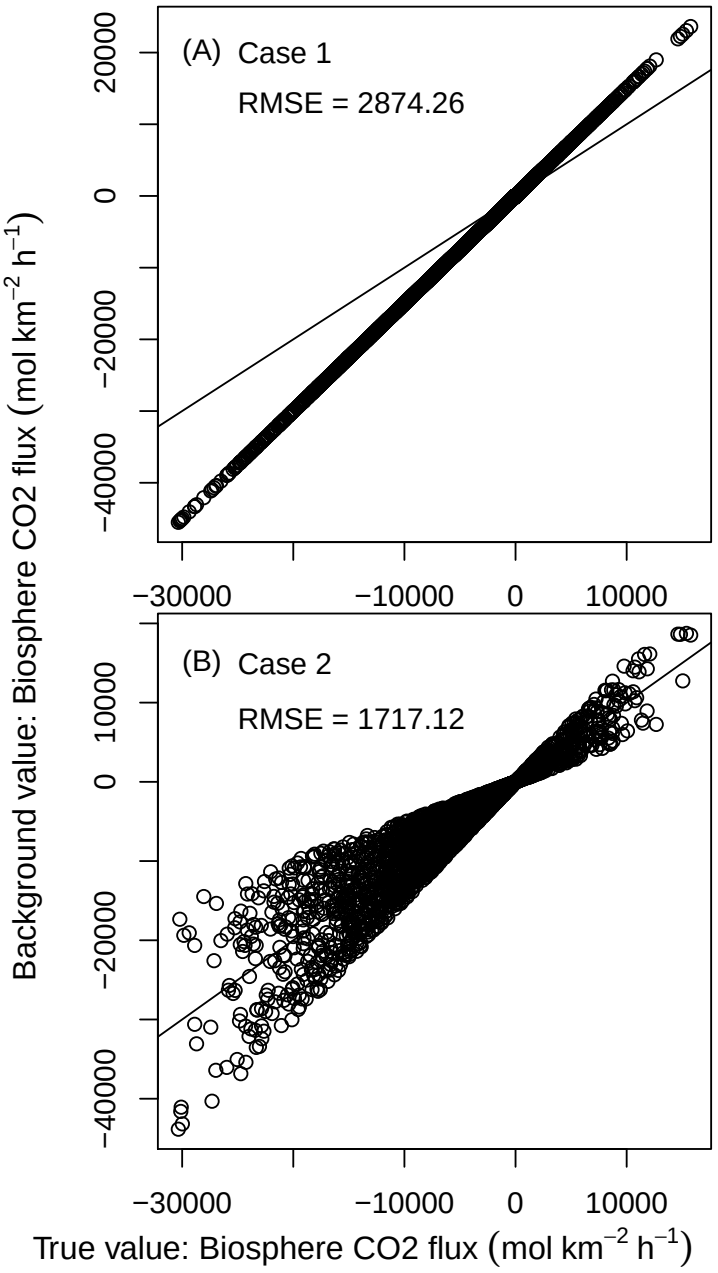

Figure 12. The first guess of biosphere CO_2 fluxes used in the two inverse experiments. The x-axis is true daily mean CarbonTracker biosphere CO_2 value (as shown in Fig 4), and y-axis is the first guess (background value). The solid line in each figure is the 1:1 line.

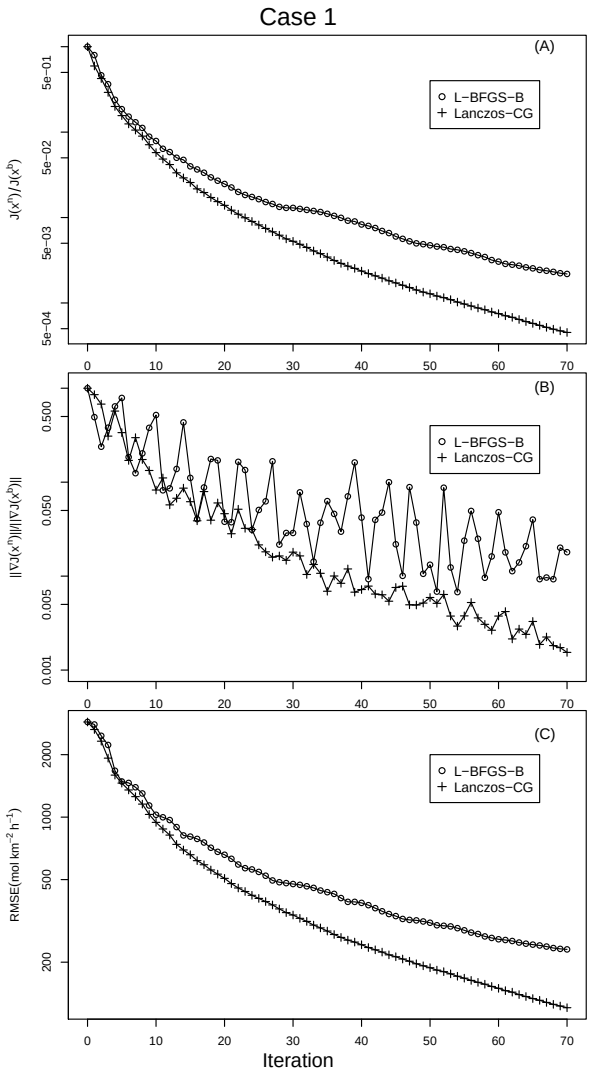

Figure 13. Results of inverse modeling experiment Case 1. Figure (a) shows the reduction of the cost function, represented by $J(x^n)/J(x^b)$. Figure (b) shows the reduction of the gradient norm, represented by $\|\nabla J(x^n)\| / \left\|\nabla J(x^b)\right\|$. Figure (c) shows the reduction of biosphere CO_2 flux RMSE.

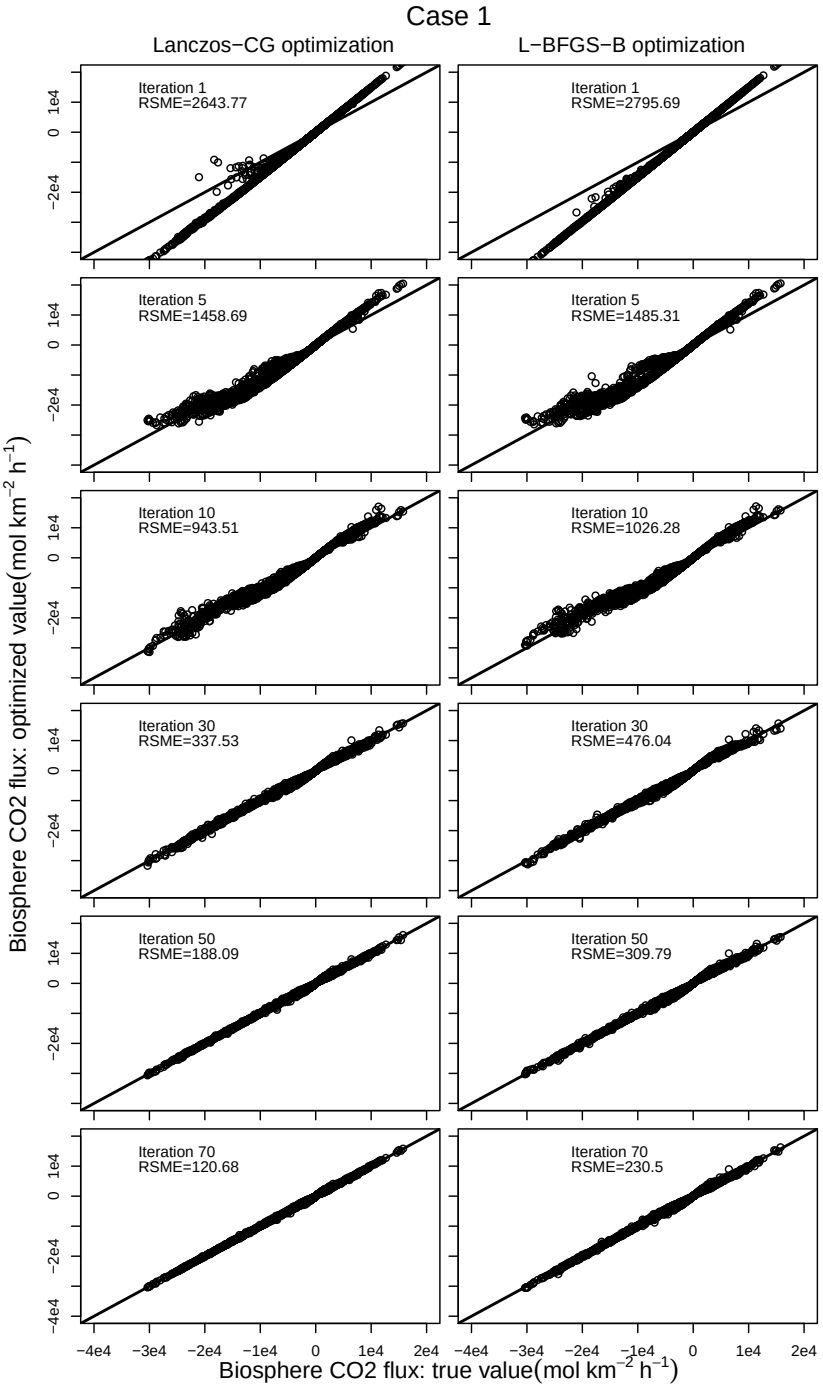

Figure 14. Comparison between the true and optimized CO_2 flux by Lanczos-CG (left column) and L-BFGS-B (right column) in inverse modeling experiment Case 1. The comparison and RMSE after the 1st 5th, 10th, 30th, 50th, 70th iteration are shown in the figure. All iterations of Lanczos-CG is from one outer loop.

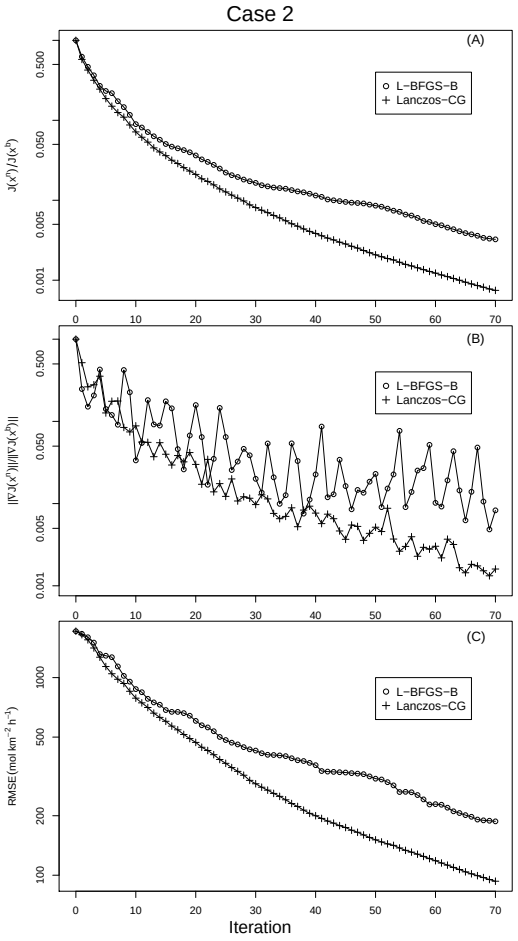

Figure 15. Same as Fig. 11, but for inverse modeling experiment Case 2.

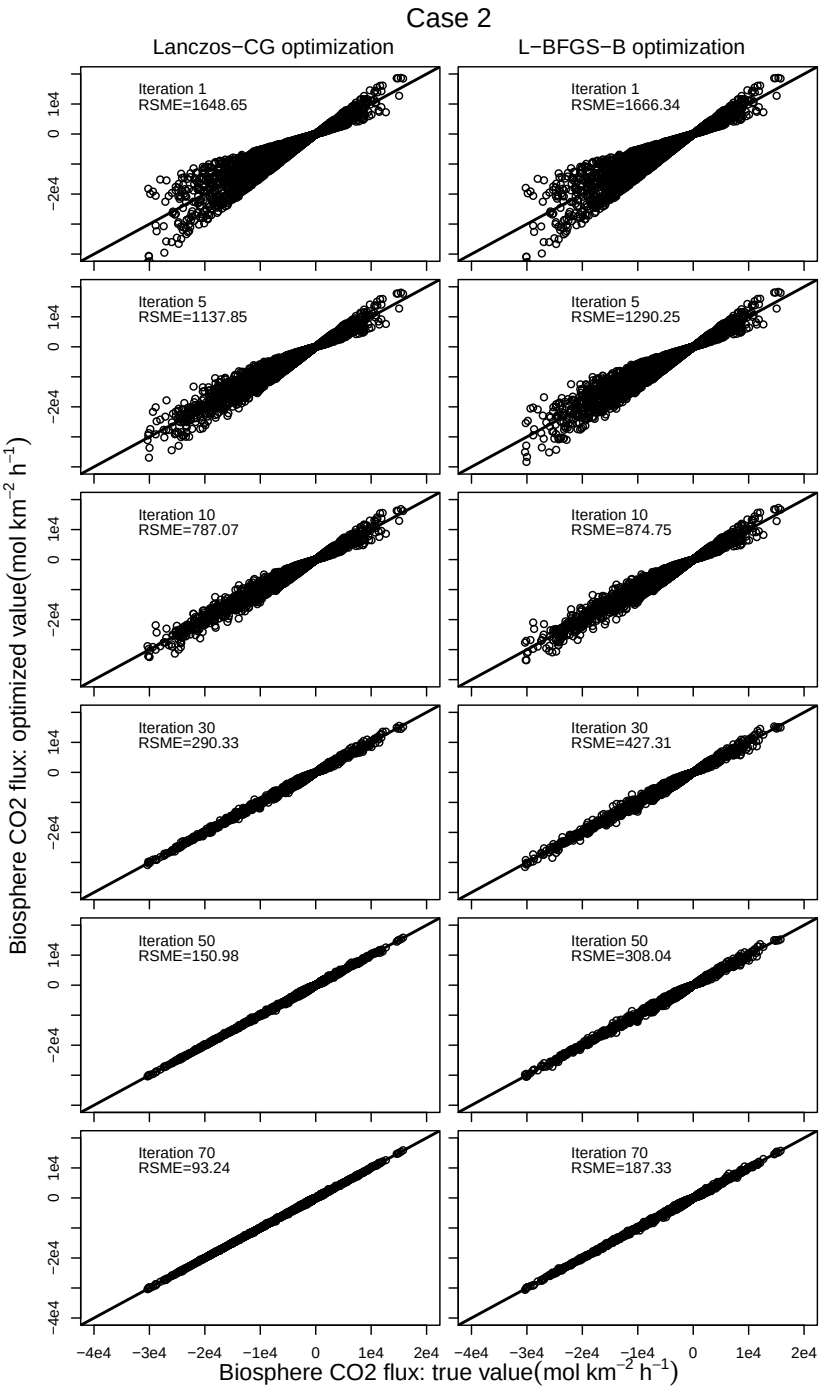

Figure 16. Same as Fig. 10, but for inverse modeling experiment Case 2.

Table 1. A list of symbols used in this article

$J(\mathbf{x})$	Cost function
$J_b(\mathbf{x})$	Background cost function
$J_o(\mathbf{x})$	Observation cost function
$\nabla J(\mathbf{x})$	Cost function gradient
$\|\nabla J(\mathbf{x})\|$	Cost function gradient norm
$\nabla^2 J(\mathbf{x})$	Cost function Hessian
$\mathbf{B}$	Background error covariance
$\mathbf{R}$	Observation error covariance
M	WRF-CO2 forward model
$\widetilde{M}$	WRF-CO2 tangent linear model
$\widetilde{M}^T$	WRF-CO2 adjoint model
H	Observation operator
$\widetilde{H}$	Tangent linear observation operator
$\widetilde{H}^T$	Adjoint observation operator
$\mathbf{k}_{co2}$	CO_2 emission scaling factor
$\mathbf{q}_{co2}$	CO_2 mixing ratio (dry air)
$g\_\mathbf{k}_{co2}$	Tangent linear variable for CO_2 emission scaling factor
$a\_\mathbf{k}_{co2}$	Adjoint variable for CO_2 emission scaling factor
$g\_\mathbf{q}_{co2}$	Tangent linear variable for CO_2 mixing ratio (dry air)
$a\_\mathbf{q}_{co2}$	Adjoint variable for CO_2 mixing ratio (dry air)
$\mathbf{x}^b$	Prior estimate of CO_2 emission scaling factor
$\mathbf{x}x^n$	Analysis of CO_2 emission scaling factor
$\hat{\mathbf{x}}$	Analysis increment of CO_2 emission scaling factor
$\mathbf{y}_k$	Observation at the k^{th} assimilation window
$\mathbf{d}_k$	Innovation vector at the k^{th} assimilation window

Table 2. Summary of variable dependence analysis for developing WRF-CO2 4DVar component models on top of WRFPLUS. In the table, an 'F' means a full physics scheme is used in the forward model, tangent linear model, or the forward sweep of the adjoint model. An 'X' means a process is not needed for CO_2 treatment. A 'Dev' means a process does not exist in WRFPLUS and has been developed for WRF-CO2 4DVar. An 'Add' means a process for CO_2 is simply added using the existing WRFPLUS code for other tracers.

Process	Forward model	Tangent linear model	Adjoint model forward sweep	Adjoint model backward sweep
Chemistry	X	X	X	X
Photolysis	X	X	X	X
Dry deposition	X	X	X	X
Wet deposition	X	X	X	X
Radiation	F	F	F	X
Surface	F	F	F	X
Cumulus	F	F	F	X
Microphysics	F	F	F	X
Advection	F	Add	F	Add
Diffusion	F	Add	F	Add
Emission	F	Dev	F	Dev
PBL	F	Dev	F	Dev
Convective transport	F	Dev	F	Dev

Table 3. WRF-CO2 4DVar model configuration and CO_2 flux used in sensitivity and inverse modeling tests.

Longwave radiation	Rapid Radiative Transfer Model (RRTM)
Shortwave radiation	Goddard shortwave
Microphysics	Thompson
Surface layer	Pleim-Xiu
Land surface	Pleim-Xiu
Planetary boundary layer	ACM2 PBL
Cumulus	Grell-Freitas
CO_2 advection	Positive-definite advection
biosphere CO_2 flux	CarbonTracker 2016
ocean CO_2 flux	CarbonTracker 2016
fire CO_2 flux	CarbonTracker 2016
fossil fuel CO_2 flux	CarbonTracker 2016

Table 4. Summary of CO_2 tower sites. Sensitivity $\partial q_{co2}/\partial k_{co2}$ as calculated by WRF-CO2 4DVar's tangent linear and adjoint models is compared against finite difference sensitivity at these sites.

Site Name	Symbol	Latitude	Longitude
Kewanee	RKW	41.28^oN	89.77^oW
Centerville	RCE	40.79^oN	92.88^oW
Mead	RMM	41.14^oN	96.46^oW
Round Lake	RRL	43.53^oN	95.41^oW
Galesville	RGV	44.09^oN	91.34^oW
Ozarks	AMO	38.75^oN	92.2^oW
WLEF	LEF	45.95^oN	9.27^oW
West Branch	WBI	41.73^oN	91.35^oW
Canaan Valley	ACV	39.06^oN	72.94^oW
Chestnut Ridge	ACR	35.93^oN	84.33^oW
Fort Peck	AFP	48.31^oN	105.10^oW
Roof Butte	AFC_RBA	36.46^oN	109.09^oW
Storm Peak Lab	SPL	40.45^oN	106.73^oW
Argle	AMT	45.03^oN	68.68^oW
Harvard Forest	HFM	42.54^oN	72.17^oW
Southern Great Plains	SGP	36.80^oN	97.50^oW
Sutro	STR	37.75^oN	122.45^oW
Hidden Peak	HDP	40.56^oN	111.64^oW
Mary's Peak	ARC_MPK	44.50^oN	123.55^oW
KWKT	KWT	31.31^oN	97.32^oW

Table 5. Summary of inverse modeling experiment results. The reductions of cost function $J(x)$, gradient norm $\|\nabla J(x)\|$, and RMSE are given as the ratio to their respective starting values. Results of the two experiment cases are values after 70 iterations.

Case 1

Reduction in	L-BFGS-B	Lanczos-CG
$J(\mathbf{x})$	2.23×10^{-3}	4.72×10^{-4}
$\|\nabla J(\mathbf{x})\|$	2.0×10^{-2}	1.7×10^{-3}
RMSE	8.01×10^{-2}	4.19×10^{-2}

Case 2

Reduction in	L-BFGS-B	Lanczos-CG
$J(\mathbf{x})$	3.31×10^{-3}	7.76×10^{-4}
$\|\nabla J(\mathbf{x})\|$	4.84×10^{-3}	1.32×10^{-3}
RMSE	1.09×10^{-1}	5.43×10^{-2}